



CHORUS

This is the accepted manuscript made available via CHORUS. The article has been published as:

Colloquium: Physical properties of group-IV monochalcogenide monolayers

Salvador Barraza-Lopez, Benjamin M. Fregoso, John W. Villanova, Stuart S. P. Parkin, and Kai Chang

Rev. Mod. Phys. **93**, 011001 — Published 10 March 2021

DOI: [10.1103/RevModPhys.93.011001](https://doi.org/10.1103/RevModPhys.93.011001)

Colloquium: Physical properties of group-IV monochalcogenide monolayers

Salvador Barraza-Lopez*

*Department of Physics,
University of Arkansas,
Fayetteville, AR 72701,
USA*

Benjamin M. Fregoso

*Department of Physics,
Kent State University,
Kent, OH 44242,
USA*

John W. Villanova

*Department of Physics,
University of Arkansas,
Fayetteville, AR 72701,
USA*

Stuart S. P. Parkin

*Max Planck Institute of Microstructure Physics,
Weinberg 2, Halle 06120,
Germany*

Kai Chang†

*Beijing Academy of Quantum Information Sciences, Beijing 100193,
China*

(Dated: September 16, 2020)

We survey the state-of-the-art knowledge of ferroelectric and ferroelastic group-IV monochalcogenide monolayers. These semiconductors feature remarkable structural and mechanical properties, such as a switchable in-plane spontaneous polarization, soft elastic constants, structural degeneracies, and thermally-driven two-dimensional structural transformations. Additionally, these 2D materials display selective valley excitations, valley Hall effects, and persistent spin helix behavior. After a description of their Raman spectra, a discussion of optical properties arising from their lack of centrosymmetry—such as an unusually strong second-harmonic intensity, large bulk photovoltaic effects, photostriction, and tunable exciton binding energies—is provided as well. The physical properties observed in these materials originate from (correlate with) their intrinsic and switchable electric polarization, and the physical behavior hereby reviewed could be of use in non-volatile memory, valleytronic, spintronic, and optoelectronic devices: these 2D multiferroics enrich and diversify the 2D materials toolbox.

CONTENTS

I. Introduction: The diversity of ultrathin ferroelectrics	2	A. Polarization switching and ultrathin memories based on in-plane ferroelectric tunnel junctions	9
II. Atomistic structure and chemical bonding of O–MXs from the bulk to MLs	3	V. Linear elastic properties, auxetic behavior, and piezoelectricity of O–MX MLs	9
III. Experimentally available O–MX MLs	7	VI. Structural degeneracies and anharmonic elastic energy of O–MX MLs	10
A. SnS MLs	7	VII. Structural phase transition and pyroelectric behavior of O–MX MLs	11
B. SnSe and SnTe MLs	7	VIII. Electronic, valley and spin properties of O–MX MLs	13
IV. Switching the direction of \mathbf{P} on O–MX MLs: demonstrating ferroelectric behavior	8	A. Electronic band structure	13
		B. Valleytronics	14
		C. Persistent spin helix behavior	15
		IX. Optical properties of O–MX MLs	16

* sbarraza@uark.edu

† changkai@baqis.ac.cn

A. Optical absorption	16
B. Raman spectra	16
C. Second harmonic generation	17
D. Bulk photovoltaic effects: injection and shift currents	18
E. Photostriction	18
F. Excitons	19
X. Summary and outlook	19
Acknowledgments	19
References	19

I. INTRODUCTION: THE DIVERSITY OF ULTRATHIN FERROELECTRICS

Ferroelectric materials display a spontaneous, intrinsic polarization \mathbf{P} that can be switched by external electric fields. The first ferroelectric material—Rochelle salt—was discovered about a century ago (Valasek, 1921). Despite a long history of applications of ferroelectrics in electric and electronic devices, the modern theory of ferroelectricity based on Berry phase—which made accurate comparisons between theory and experimental measurements possible—was not established until the 1990s (King-Smith and Vanderbilt, 1993; Resta, 1994); see Ref. (Rabe *et al.*, 2007) for more details. From that point on, deep connections of this field with the geometry and topology of quantum mechanical wave functions have been pointed out (Bernevig and Hughes, 2013; Vanderbilt, 2018). Ferroelectric behavior is relevant from both a fundamental physical perspective as well as applications, and this Colloquium was written to highlight the physical properties of 2D ferroelectric and ferroelastic materials within the group-IV monochalcogenide family (Littlewood, 1980).

Researchers have always wondered whether there is a critical thickness for ferroelectric behavior below which polarization switching becomes suppressed (Rabe *et al.*, 2007). Considering non-layered ferroelectric films with an out-of-plane intrinsic polarization \mathbf{P} , it was initially thought that the depolarization field arising from an incomplete cancellation of the space charge and an out-of-plane polarization charge at an electrode-ferroelectric interface [see, *e.g.*, Refs. (Black *et al.*, 1997; Janovec, 1959; Mehta *et al.*, 1973; Merz, 1956; Triebwasser, 1960)] would raise the total energy of the system and eventually suppress the polarized state. Nevertheless, and as growth techniques for thin films developed, the experimentally extracted critical thickness of ferroelectric thin films decreased from over 100 nm (Feuersanger *et al.*, 1964) to tens of nanometers (Slack and Burfoot, 1971; Tomashpolski, 1974; Tomashpolski *et al.*, 1974), and eventually to only a few unit cells (u.c.s) (Bune *et al.*, 1998; Tybell *et al.*, 1999). The behavior of ultrathin ferroelectric films has been predicted to high precision by first principles calculations, suggesting critical thicknesses of several

u.c.s for certain materials (Gerra *et al.*, 2006; Junquera and Ghosez, 2003; Meyer and Vanderbilt, 2001; Sai *et al.*, 2005; Wu *et al.*, 2004; Zembilgotov *et al.*, 2002), or single-u.c. thickness for others (Almahmoud *et al.*, 2010, 2004; Sai *et al.*, 2009; Zhang *et al.*, 2014). Concurrently, sophisticated experiments on select compounds [PbTiO₃ (3 u.c.s) (Fong *et al.*, 2006, 2004), BaTiO₃ (4 u.c.s) (Tenne *et al.*, 2006, 2009), PbZr_{0.2}Ti_{0.8}O₃ (1.5 u.c.s) (Gao *et al.*, 2017), YMnO₃ (2 u.c.s) (Nordlander *et al.*, 2019), and BiFeO₃ (1 u.c.) (Wang *et al.*, 2018a)] continue to push the critical thickness toward the single u.c. limit.

Meanwhile, a series of ultra-thin *layered* ferroelectric materials—especially attractive for the design and fabrication of functional (van der Waals) heterostructures—have been experimentally discovered, including In₂Se₃ (Cui *et al.*, 2018a; Ding *et al.*, 2017; Poh *et al.*, 2018; Wan *et al.*, 2018; Xiao *et al.*, 2018; Xue *et al.*, 2018a,b; Zheng *et al.*, 2018; Zhou *et al.*, 2017), CuInP₂S₆ (Deng *et al.*, 2019; Liu *et al.*, 2016), BA₂PbCl₄ (Liao *et al.*, 2015; You *et al.*, 2018), d1T-MoTe₂ (Yuan *et al.*, 2019), 1T-WTe₂ (Fei *et al.*, 2018) [which is also a quantum spin Hall material (Asaba *et al.*, 2018; Fei *et al.*, 2017; Qian *et al.*, 2014; Song *et al.*, 2018; Tang *et al.*, 2017; Wu *et al.*, 2018)], and of course, monolayers (MLs) of group-IV monochalcogenides like SnS, SnSe and SnTe. A brief and experimentally-driven summary of layered ferroelectrics is provided in Table I.

The discovery of 2D and layered ferroelectrics facilitates the design of future non-volatile devices that are fully made of 2D material heterostructures. The experimentally verified 2D ferroelectric materials exhibit both out-of-plane and in-plane switchable spontaneous polarizations in few-layer films and at room temperature. Some prototype devices have also been demonstrated. For example, a ferroelectric diode in a graphene/ α -In₂Se₃ heterostructure has a relatively low coercive field of 200 kV/cm, and an electric current on/off ratio of $\sim 10^5$ (Wan *et al.*, 2018). A d1T-MoTe₂ ferroelectric tunneling junction yielded an electric current on/off ratio of 1,000 (Yuan *et al.*, 2019).

Among all ultrathin ferroelectrics, a family of ferroelectric semiconductors with moderate band gaps known as group-IV monochalcogenide MLs—and referred to as *MX* MLs henceforth—exhibit outstanding properties that are promising for many applications. By far, they are the only family of 2D ferroelectrics experimentally shown to display a robust and switchable in-plane spontaneous polarization at the limit of a single van der Waals ML at room temperature. Furthermore, many intriguing physical behaviors have been theoretically predicted in *MX* MLs such as selective valley excitations, valley Hall effects, persistent spin helix behavior, *etc.*

Nevertheless, and despite of these attractive theoretical predictions, the experimental growth and characterization remains difficult, partly because of reduced sample dimensions. Therefore, reviewing the current achieve-

TABLE I Experimentally reported layered ferroelectrics, including the space group of the ferroelectric phase, its intrinsic and switchable polarization [in-plane (IP) and out-of-plane (OOP)], preparation methods employed, the critical temperature above which a paraelectric phase ensues, the coercive field E_c (thicknesses for which T_c and E_c were determined are added in parenthesis), and other related properties. If the space group was not specified in the source literature, a prefix “d-” (for *distorted*) was added in front of the space group of the corresponding undistorted high-symmetry structure. ML stands for monolayer. P stands for spontaneous polarization.

Material	Space group	P direction	Preparation ^a	T_c (K)	E_c (kV/cm)	Other properties
α -In ₂ Se ₃	$R3m$	IP + OOP	ME	700 (4 ML)	200 (5 nm)	$d_{33} = 0.34$ pm/V ^b (1 ML)
β' -In ₂ Se ₃	d- $R\bar{3}m$	IP	ME	> 473 (100 nm)		
CuInP ₂ S ₆	Cc	IP + OOP ^c	ME	> 320 (4 nm)		
BA ₂ PbCl ₄	$Cmc2_1$	IP	ME	> 300 (2 ML)	13 (bulk)	$P \sim 13$ μ C/cm ²
d1T-MoTe ₂	d- $P\bar{3}m$	OOP	ME, MBE	330 (1 ML)		
1T'-WTe ₂	$Pnm2_1$	OOP	ME	350 (2–3 ML)		$P \neq 0$ only when ≥ 2 ML
SnS odd-ML	$P2_1mn$	IP	MBE, PVD	> 300 (1–15 ML)	10.7/25 (1/9 ML)	
SnSe ML	$P2_1mn$	IP	MBE	380~400 (1 ML)	140 (1 ML)	
SnTe ML	$P2_1mn$	IP	MBE	270 (1 ML)		

^a MBE, molecular beam epitaxy; ME, mechanical exfoliation; PVD, physical vapor deposition

^b Piezoelectric coefficient

^c Vanishing in-plane polarization below a critical thickness of 90–100 nm.

ments and spurring a broader interest in this field provided the motivation to write this Colloquium. Despite the existence of several reviews focusing on the computational (Cui *et al.*, 2018b; Wu and Jena, 2018), experimental/computational (Guan *et al.*, 2019), and experimental/theoretical (Titova *et al.*, 2020) aspects of 2D ferroelectrics, an all-encompassing review dedicated to the physical behavior of MX MLs is still missing.

The structure of this Colloquium is as follows. The atomistic structure of MX s in the bulk and MLs is discussed in Sec. II. Atomistic coordination, the nature of their chemical bond, group symmetries, order parameters, as well as unexpected atomistic configurations experimentally obtained are covered in this Section. Sec. III introduces the three members of this family (SnS, SnSe, and SnTe) that have been grown at the ML limit. Experimental characterization, including the verification of polarization at exposed edges in ML nanoplates, can be found there as well. The experimental ferroelectric switching of SnS, SnSe, and SnTe MLs is discussed in Sec. IV; novel memory concepts based on an in-plane ferroelectric switching are also introduced in that Section.

Linear elastic properties, structural degeneracies, and finite temperature thermal behavior (including phase transitions) are covered in Secs. V, VI, and VII, respectively. In a nutshell, MX MLs are much softer than graphene, hexagonal boron nitride MLs, and transition metal dichalcogenide (TMDC) MLs. Their linear elastic properties, unusually large piezoelectric coefficients, and auxetic behavior are described in Sec. V. The elastic energy landscape is introduced in Sec. VI, which permits understanding the structural degeneracies of these 2D ferroelectrics, and the structural phase transitions that are discussed in Sec. VII.

Electronic and optical properties of MX MLs are the

subjects of Secs. VIII and IX. The electronic properties are discussed in a gradual manner that includes band structures and valley properties without spin-orbit coupling, and a subsequent exposition of (spin-enabled) persistent spin helix behavior. Optical properties include the anisotropic absorption spectra, Raman spectra, SHG, injection and shift currents, photostriction, and excitonic effects. A summary and outlook is presented in Sec. X.

A unified and consistent notation has been deployed to streamline the discussion. In particular, the choice of crystallographic axes is such that orthogonal lattice vectors $\mathbf{a}_{1,0}$, $\mathbf{a}_{2,0}$, and $\mathbf{a}_{3,0}$ correspond to crystallographic vectors \mathbf{a} , \mathbf{b} , and \mathbf{c} and point along the x -, y -, and z -direction, respectively [\mathbf{a}_1 (\mathbf{a}_2) is the so-called arm-chair (zigzag) direction]. These choices will lead to a modification of space group labeling, a redefinition of high-symmetry points in the electronic band structure, and to the relabeling of tensors from some of the source literature. The benefit from this effort is a self-contained discussion that is not interrupted from a lack of a standard notation. In addition, given that the structure of these materials evolves as a function of mechanical strain, temperature, electric field, and optical illumination, structural variables with a zero subindex represent their value on a ground state configuration at zero temperature and without external perturbations.

II. ATOMISTIC STRUCTURE AND CHEMICAL BONDING OF O- MX S FROM THE BULK TO MLs

Group-IV monochalcogenides are binary compounds with a chemical formula MX , where M is a group IVA element and X belongs to group VIA in the Periodic Table. Even though carbon, silicon, lead, oxygen, and even polonium belong to these groups, MX compounds

containing these elements will not be discussed here for the following reasons: SiS MLs possess a ground state structure with $Pma2$ symmetry (Yang *et al.*, 2016) which lacks a net intrinsic electric polarization; see Ref. (Kamal *et al.*, 2016) concerning a lower-energy structure for 2D SiSe, too. PbX compounds lack a net \mathbf{P} regardless of the number of layers (more on this later). Similarly, materials such as 2D SiO, GeO, and SnO display a non-ferroelectric litharge structure (Kamal *et al.*, 2016; Lefebvre *et al.*, 1998). This way, M will either be germanium (Ge) or tin (Sn) while X represents sulphur (S), selenium (Se), or tellurium (Te) in what follows.

GeTe and SnTe are rhombohedral (R-phase) and GeS, GeSe, SnS, and SnSe turn orthorhombic (O-phase) in the bulk (Littlewood, 1980). As illustrated in Fig. 1(a), O- MX compounds have a layered structure. One ML refers to a van der Waals layer [or two atomic layers (2 ALs)] or half of an O- MX u. c.

Strictly speaking, the intrinsic switchable polarization \mathbf{P} should not be showcased as a vector on periodic structures. Therefore, in certain theoretical discussions, we will utilize an order parameter \mathbf{p}_0 (parallel to \mathbf{P}) that remains well-defined on periodic structures. The letter p stands for *projection*, and this order parameter is defined in the next paragraph.

Consider the vector \mathbf{r}_{XM} starting at X atom 1 and ending at the nearest M atom (atom 2) in the lower ML seen in Fig. 1(a). The positions of the remaining two atoms within the lower ML (3 and 4) are obtained by a screw operation about the x -axis, or by a diagonal (n) glide operation about the z -axis applied to \mathbf{r}_{XM} . Calling \mathbf{r}'_{XM} the vector starting at (X) atom 3 and ending at (M) atom 4, we define $\mathbf{p}_0 = \mathbf{r}_{XM} + \mathbf{r}'_{XM}$. The mirror symmetry along the $x-z$ plane makes $\mathbf{p}_0 \cdot \hat{y} = 0$, while the screw operation renders $\mathbf{p}_0 \cdot \hat{z} = 0$, so that \mathbf{p}_0 is parallel to the longer lattice vector $\mathbf{a}_{1,0}$. These symmetries also render a zero intrinsic polarization along the y - and z -directions. Ferroelectric O- MX MLs belong to space group 31 (Kamal *et al.*, 2016; Rodin *et al.*, 2016) [usually written as $Pnm2_1$ but labeled $P2_1mn$ for lattice vectors as drawn in Fig. 1(c)], and a top view of their anisotropic u. c. is provided in Fig. 1(c) within solid lines. Phonon dispersion calculations demonstrate the structural stability of these MLs (Singh and Hennig, 2014). A zero value of the *order parameter* θ in a ML with dissimilar lattice constants ($a_{1,0} \neq a_{2,0}$) leads onto a paraelectric structure with $\mathbf{p} = \mathbf{0}$ belonging to symmetry group 59 ($Pm\bar{m}n$).

The alternating direction of \mathbf{p}_0 (or antipolar coupling) within each ML arises from the inversion center shown in the side view along the $x-z$ plane in Fig. 1(a) (the atoms related by inversion are joined by dash-dot lines). Bulk O- MX s belong to space group 62 [$Pnma$ (Gomes and Carvalho, 2015), or $Pcmn$ with the lattice vectors employed here]. The side view of the u. c. boundaries in solid line, interatomic distances $d_{1,0} < d_{2,0} < d_{3,0}$, a tilt angle θ_0 ,

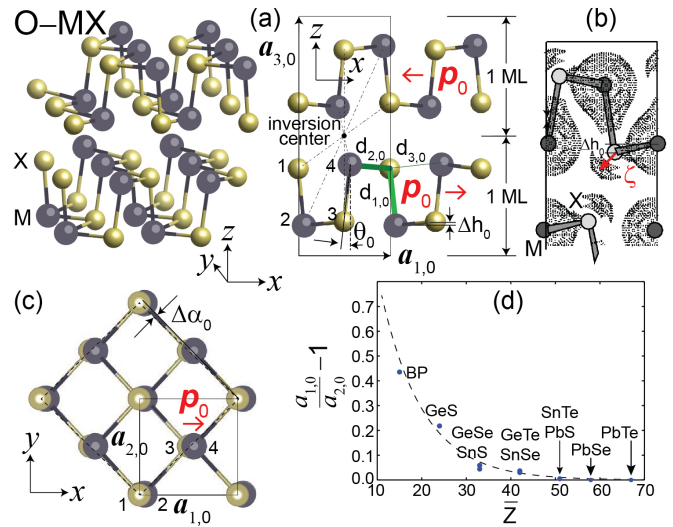


FIG. 1 (a) Structure of bulk O- MX s, with the M atom shown in dark gray (big circles) and the X atom in yellow (light gray, small circles). Left: 3D view of two MLs with antiparallel polarization. Right: side view along the $x-z$ plane showing $\mathbf{a}_{1,0}$ and $\mathbf{a}_{3,0}$ lattice vectors ($\mathbf{a}_{2,0}$ points into the page). The inversion center swaps the direction of \mathbf{p}_0 at consecutive MLs (red arrows), and $p_0 = |\mathbf{p}_0| \propto \theta_0$. Interatomic distances $d_{1,0}$, $d_{2,0}$, and $d_{3,0}$ as well as Δh_0 are shown, too. (b) Electronic density showing a lone pair ζ , and Δh_0 . Dark (light) circles stand for tin (sulfur or selenium). Adapted from Ref. (Lefebvre *et al.*, 1998) with permission. Copyright, 1998, American Physical Society. (c) Top view of a O- MX ML. $\Delta\alpha_0$ measures the deviation from 90° of the rhombus highlighted by dashed lines; $\Delta\alpha_0 = 0$ when $a_{1,0} = a_{2,0}$. (d) The $a_{1,0}/a_{2,0}$ ratio (proportional to $\Delta\alpha_0$) is tunable by the compound's average atomic number \bar{Z} . Adapted from Ref. (Mehboudi *et al.*, 2016a) with permission. Copyright, 2016, American Chemical Society.

and the height Δh_0 of an X atom relative to its nearest M atom (Kamal *et al.*, 2016). A net switchable \mathbf{P}_0 ensues in binary compounds lacking inversion symmetry, which is the case for individual MLs of O- MX s (Fei *et al.*, 2015; Gomes and Carvalho, 2015; Gomes *et al.*, 2015; Singh and Hennig, 2014; Tritsaris *et al.*, 2013; Zhu *et al.*, 2015). The atomistic structure and the in-plane \mathbf{p}_0 of O- MX MLs can be understood on the basis of the chemistry of black phosphorus (BP) MLs as follows.

Carbon belongs to group IVA and graphite has four valence electrons and an sp^2 hybridization. Phosphorus (P) belongs to group VA, and black phosphorus has five valence electrons and displays an sp^3 hybridization (Kamal *et al.*, 2016). In (three-fold coordinated) graphite, three atoms form strong (σ) in-plane bonds and the fourth (π) electron protrudes out of plane. BP is three-fold coordinated as well, having its closest neighboring atom at a distance d_1 and two additional atoms located at a slightly larger distance d_2 . Given that a phosphorus atom contains five valence electrons, such three-fold coordination requires the existence of two additional non-bonded

TABLE II Interatomic distances in bulk SnS and SnSe. N is the number of neighbors at any given distance. Taken from Ref. (Lefebvre *et al.*, 1998).

Material atoms	d (Å)	N	Material atoms	d (Å)	N
SnS	Sn-S	2.63 ($d_{1,0}$)	SnSe	Sn-Se	2.74 ($d_{1,0}$)
		2.66 ($d_{2,0}$)			2.79 ($d_{2,0}$)
		3.29 ($d_{3,0}$)			3.34 ($d_{3,0}$)
		3.39			3.47
		3.49			3.55
	Sn-Sn	2		Sn-Sn	2
	S-S	4		Se-Se	4
		3.90			3.94

electrons [known as a *lone pair* (ζ)] per atom. Unlike graphene, which maintains a planar configuration with two atoms in its u. c., lone pairs confer BP MLs with a puckered structure and a rectangular u. c. containing four atoms.

Similar to hexagonal boron nitride—which is made out of a group IIIA element (B) and a group VA element (N) and is isostructural to graphite—Fig. 1(a) indicates that O- MX s are isostructural to BP. Table II shows that bulk SnS has similar distances d_1 and d_2 for a three-fold atomistic coordination, and the same can be said of interatomic distances in bulk SnSe, also listed in the Table. The equivalent to a lone pair ζ is assigned to the more negatively charged X atom in Fig. 1(b) (Lefebvre *et al.*, 1998). The reader may notice that Δh_0 is positive in Fig. 1(a) and negative in Fig. 1(b): its sign determines certain elastic properties that will be discussed in Sec. V.

The rhombic distortion angle $\Delta\alpha_0$ (Chang *et al.*, 2016) shown in Fig. 1(c) indicates the anisotropy of the u.c. and is related to the ratio of lattice constants $a_{1,0}/a_{2,0}$ as follows (Barraza-Lopez *et al.*, 2018):

$$\frac{a_{1,0}}{a_{2,0}} = \frac{1 + \sin \Delta\alpha_0}{\cos \Delta\alpha_0}, \quad (1)$$

or $\Delta\alpha_0 \simeq \frac{a_{1,0}}{a_{2,0}} - 1$ for small angles when $\Delta\alpha_0$ is expressed in radians.

Letting Z_M (Z_X) be the atomic number of atom M (X) and defining the average atomic number $\bar{Z} = (Z_M + Z_X)/2$, Fig. 1(d) illustrates a decaying exponential dependence of $\frac{a_{1,0}}{a_{2,0}} - 1$ on \bar{Z} (Mehboudi *et al.*, 2016a). $\frac{a_{1,0}}{a_{2,0}} - 1$ has been called the *reversible strain* (Wu and Zeng, 2016) or *tetragonality ratio*, and it correlates with P_0 in bulk ferroelectrics (Lichtensteiger *et al.*, 2005). Fig. 1(d) indicates that—at zero temperature—lattice vectors turn more equal (unequal) on heavier (lighter) MX MLs. Having equal lattice vectors, Fig. 1(d) shows that Pb-based MX MLs are paraelectric [$P_0 = 0$; a behavior experimentally confirmed on PbTe MLs; see Supporting Information in Ref. (Chang *et al.*, 2016)] and are not discussed here for that reason. Ferroelectric O- MX MLs with $a_{1,0} \neq a_{2,0}$ have similar structures and hence display similar physical behavior; this observation will

TABLE III Net charge transfer ΔQ (in e) from atom M to atom X and change in electronegativity $\Delta\xi = \xi_X - \xi_M$ (in eV) for O- MX MLs. Taken from Ref. (Kamal *et al.*, 2016).

Material	\bar{Z}	ΔQ	$\Delta\xi$	Material	\bar{Z}	ΔQ	$\Delta\xi$
GeS ML	24	0.815	0.57	SnS ML	33	0.980	0.62
GeSe ML	33	0.649	0.54	SnSe ML	42	0.855	0.59
GeTe ML	42	0.372	0.09	SnTe ML	51	0.596	0.14

permit drawing meaningful comparisons between different experimental and theoretically studied compounds within this material family.

Continuing the discussion of chemistry, one observes in Table III a correlation between the charge transfer ΔQ [or *ionicity* (Littlewood, 1980)] from the group IVA element onto the one belonging to group VIA, and Pauling’s difference in electronegativity $\Delta\xi$. Although an interplay among covalent, ionic, and resonant bonding has been argued to describe MX s, a new type of bonding (called *metavalent*, and thought of as a combination of ‘metallic’ and ‘covalent’) has been proposed to classify these materials (Kooi and Wuttig, 2020; Raty *et al.*, 2019; Ronneberger *et al.*, 2020). Variables employed to identify the appropriate type of bonding include the coordination number, the electronic conductivity, the dielectric constant ϵ_∞ , the bond polarizability, and the lattice anharmonicity. Setting up a two-dimensional map where the horizontal axis is the charge transfer ΔQ and the vertical axis (named *electron sharing*) is a measure of electronic exchange and correlation (Raty *et al.*, 2019), metavalent compounds sit in between covalently-bonded and metallic materials. In the bulk, materials such as GeS, GeSe, SnS, and SnSe are assigned a covalent bonding, while GeTe can display either covalent or metavalent bonding depending on its phase [R and cubic (C) phases being metavalent and the O phase being covalent]; bulk SnTe, PbS, PbSe, and PbTe are assigned a metavalent character (Kooi and Wuttig, 2020; Raty *et al.*, 2019).

The in-plane u. c. area (*i.e.*, $|\mathbf{a}_{1,0} \times \mathbf{a}_{2,0}|$) of O- MX s is a function of the number of MLs (Dewandre *et al.*, 2019; Hu *et al.*, 2015; Poudel *et al.*, 2019; Ronneberger *et al.*, 2020; Yang *et al.*, 2018), a feature observed in BP as well (Shulenburg *et al.*, 2015) that is related to the thickness-dependent spatial distribution of lone pairs. Such a dependence of $|\mathbf{a}_{1,0} \times \mathbf{a}_{2,0}|$ on thickness is not observed in more traditional 2D materials such as graphene and TMDCs.

Leaving a detailed discussion of ultrathin film creation and characterization to Sec. III, Figs. 2(a) and 2(b) display few-ML SnS and SnTe films and provide striking examples of unexpected structure: indeed, while bulk SnS displays the $Pcmn$ group symmetry, SnS grown on mica can take on a *ferroelectrically-coupled* (sometimes labeled AA) stacking sequence for up to fifteen MLs (Higashitarumizu *et al.*, 2020) [Fig. 2(a)], with a $Pcmn$

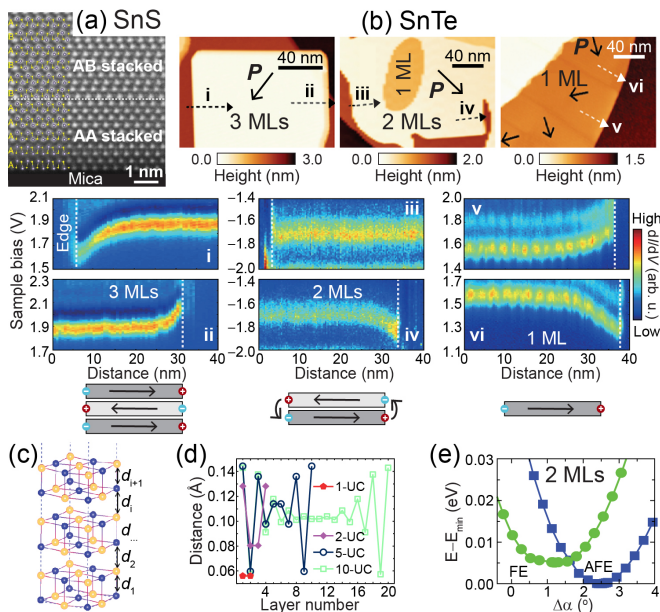


FIG. 2 (a) Cross-sectional STEM images of few-ML SnS grown on mica exhibit ferroelectric coupling for up to 15 MLs. Reproduced from Ref. (Higashitarumizu *et al.*, 2020) under the terms of the CC-BY Attribution License. Copyright, 2020, Springer Nature. (b) Ultrathin SnTe grown on epitaxial graphene develops an antiferroelectric coupling, as demonstrated by band bending at the exposed edges of few-layer nanoplates (subplots i through vi). Lowermost diagrams indicate electrostatic interactions at exposed edges upon antiferroelectric coupling. Reproduced from (Chang *et al.*, 2019a) with permission. Copyright, 2019, John Wiley and Sons. (c and d) Demonstration of layering in ferroelectrically-coupled ultrathin SnTe by the uneven distance d_i among layers. Reproduced from (Yang *et al.*, 2018) and (Liu *et al.*, 2018) with permission. Copyright, 2017, American Institute of Physics and 2018, American Physical Society. (e) A SnTe bilayer with antiferroelectric (AFE) coupling has a lower total energy when compared to a ferroelectric (FE) coupled one. Reproduced from (Kaloni *et al.*, 2019) with permission. Copyright, 2019, American Physical Society.

group symmetry acquired by subsequent MLs on thicker films. Non-polar, thick SnS can be switched into a ferroelectric phase by an external electric field (Bao *et al.*, 2019). Additional experimental MX morphologies include GeS nanowires created along an axial screw dislocation (Sutter *et al.*, 2019) and the antiferroelectrically-coupled ultrathin SnTe grown on (metallic) epitaxial graphene (Chang *et al.*, 2019a) that is discussed next.

Bulk SnTe displays a metavalent, R-phase in the bulk. Grown on a metallic substrate, ultrathin SnTe flakes with a 3-ML, bilayer, or ML thicknesses were characterized with a scanning tunneling microscope (STM), which permits elucidating their in-plane polarization \mathbf{P} switching from the band bending of the conduction band edge observed in Fig. 2(b). These STM spectra were captured along the dashed straight lines at subplots (i) through

(vi) in Fig. 2(b) cutting through the nanoplates' edges (Chang *et al.*, 2019a, 2020, 2016). (Additional details on the determination of \mathbf{P} will be provided in Sec. III.) Band bending is almost non-existent in SnTe bilayers, which implies an antipolar coupling among MLs, and shows that the bonding of SnTe transitions from metavalent in the bulk to covalent in ultrathin films (Ronneberger *et al.*, 2020).

Three theoretical works (Liu *et al.*, 2018; Ronneberger *et al.*, 2020; Yang *et al.*, 2018) explain the layered nature of ultrathin SnTe. They were performed using either the local density approximation [LDA (Perdew and Zunger, 1981)] or the generalized gradient approximation as implemented by Perdew, Burke, and Ernzerhof [PBE (Perdew *et al.*, 1996)] for exchange-correlation (XC) within density-functional theory (Martin, 2004) and assume a bulk-like (*i.e.*, ferroelectric) stacking of successive MLs in freestanding SnTe configurations as the one depicted in Fig. 2(c).

Bulk SnTe features a Peirels distortion—a result of the competition among electron delocalization and localization (Ronneberger *et al.*, 2020)—that creates a net polarization along its diagonal and distorts a cubic lattice into a rhombohedral one. As a result: (i) a bulk u. c. has both an in-plane and an out-of-plane intrinsic polarization and, considering two atomic layers as a ML, (ii) consecutive MLs are coupled ferroelectrically. This is different to $O-MX$ s, compounds with no net out-of-plane polarization and an antipolar coupling among successive MLs; see Fig. 1(a). Nevertheless, the depolarization field quenches the out-of-plane polarization of SnTe films (Liu *et al.*, 2018), creating an in-plane lattice expansion (Yang *et al.*, 2018) and a separation between MLs resulting in the layered structure seen in Fig. 2(d). Freestanding SnTe films with ferroelectric coupling have an intrinsically higher T_c than their bulk counterpart due to an interplay among hybridization interactions and Pauli repulsion. Additionally, electron sharing (Raty *et al.*, 2019) increases with decreasing thickness, imparting chemical bonds with a more covalent character (Ronneberger *et al.*, 2020).

Most computational works on MX s that employ density-functional theory make use of the PBE approximation (Perdew *et al.*, 1996) to XC. Yet, and as seen in Fig. 2(e), the experimentally observed antipolar coupling and the magnitude of $\Delta\alpha$ on bilayer SnTe films is recovered when using self-consistent van der Waals [vdW-DF-cx (Berland and Hyldgaard, 2014)] interactions (Kaloni *et al.*, 2019). In any case, Figs. 2(a) and 2(b) indicate that the details of the initial surface are crucial for the type of atomistic structure formed by ultrathin MX films (Kooi and Wuttig, 2020).

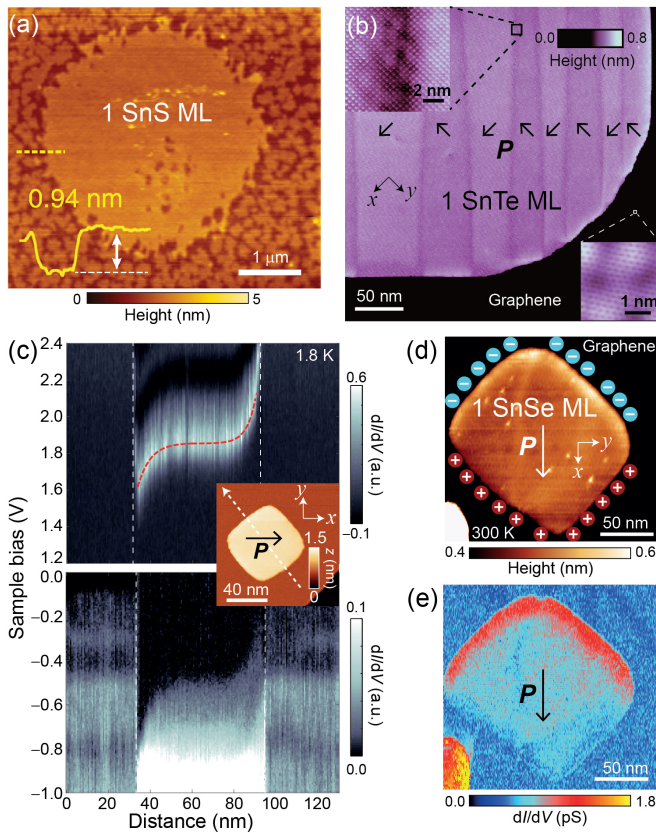


FIG. 3 (a) Atomic force microscopy topographic image of a SnS ML on mica. Reproduced from Ref. (Higashitarumizu *et al.*, 2020) under the terms of the CC-BY Attribution License. Copyright, 2020, Springer Nature. (b) STM topography of a SnTe ML nanoplate on epitaxial graphene, with head-to-tail 90° domains having an intrinsic polarization \mathbf{P} indicated by arrows. Adapted from Ref. (Chang *et al.*, 2016). Copyright, 2016, American Association for the Advancement of Science. (c) Low temperature dI/dV spectra across the dashed arrow in the inset for a SnSe ML nanoplate on graphene. (c and d) Room temperature STM topography and dI/dV : higher dI/dV implies a larger electronic charge. Taken from Ref. (Chang *et al.*, 2020) under the terms of the CC-BY Attribution License. Copyright, 2020, American Chemical Society.

III. EXPERIMENTALLY AVAILABLE O-*MX* MLs

A. SnS MLs

Room-temperature in-plane ferroelectricity was demonstrated in few-ML SnS by a combination of piezo-force microscopy (PFM), second harmonic generation (SHG), and electric transport experiments (Bao *et al.*, 2019). In order to overcome PFM’s weakness in detecting the in-plane polarization of O-*MX*s, SnS films were grown by molecular beam epitaxy (MBE) on corrugated graphite substrates so that \mathbf{P} was not perfectly perpendicular to the PFM tip and a finite polarization signal could be picked up. Ferroelectric

domains and PFM hysteresis loops were resolved on 10 nm thick SnS films grown on mica, and a SHG signal was collected, too. The modification of film morphology illustrates the difficulties of traditional techniques such as PFM to characterize ultrathin ferroelectric films with an in-plane \mathbf{P} switching, and the need to develop new techniques to characterize these ferroelectrics without changing morphology. Two-terminal devices were fabricated on a 15 nm thick SnS film grown on mica which was subsequently transferred onto a doped Si substrate covered by 300 nm thick SiO_2 . Hysteresis was found in the $I - V$ curves with a coercive field of 10.7 kV/cm and a maximum I_{on}/I_{off} ratio of ~ 100 . Furthermore, the remnant polarization increased when a negative gate voltage was applied (Bao *et al.*, 2019).

The creation and characterization of SnS MLs was recently reported (Higashitarumizu *et al.*, 2020). SHG signals—a signature of lack of inversion symmetry and ferroelectricity that will be discussed from a combined theory/experiment perspective in Sec. IX.C—were detected in SnS ML flakes grown *via* physical vapor deposition (PVD) on (insulating) mica. Two-terminal devices patterned onto these as-grown flakes display hysteresis in $I - V$ loops—yet another signature of ferroelectricity that will be discussed in Sec. IV. Consistent with the ML arrangement depicted in Fig. 2(a), ferroelectricity is detected in SnS films composed of up to fifteen MLs, *including those composed of an even number of MLs*. Ferroelectricity is unexpected in even-ML O-*MX* films because they are assumed to be centrosymmetric, lacking a net polarization according to the $Pcmn$ group symmetry. A coercive field of 25 kV/cm was found for 9-ML thick SnS by electric transport measurements. An apparent remnant polarization as large as $P_r \sim 3 \mu\text{C}/\text{m}$ was experimentally determined, much larger than the theoretical value of 240–265 pC/m listed in Table IV, and probably an artifact due to the relatively high conductance of SnS.

B. SnSe and SnTe MLs

The first experimentally discovered 2D ferroelectric in the O-*MX* family is the SnTe ML grown by MBE on (metallic) graphene (Chang *et al.*, 2016; Chang and Parkin, 2019) and characterized by STM (Chang *et al.*, 2019a, 2016, 2019b) in Fig. 3(b). As seen in Figs. 3(c) and 3(d), SnSe MLs have been grown by MBE on graphene, too (Chang *et al.*, 2020). Due to the metallic substrate in which these are grown, the techniques employed to characterize ultrathin SnSe and SnTe films are different and complementary to those employed for SnS. Although STM is an unconventional tool to study ferroelectrics, its extreme surface sensitivity and access to the materials’ local electronic structure are advantageous for studying ultrathin ferroelectric flakes with an in-plane intrinsic polarization, where PFM lacks sensitivity and may

TABLE IV Spontaneous in-plane polarization P_0 (in pC/m) as determined by DFT with the PBE XC functional.

Material	\bar{Z}	P_0^a	P_0^b	P_0^c	Material	\bar{Z}	P_0^a	P_0^b	P_0^c
GeS ML	24	484	480	486	SnS ML	33	260	240	265
GeSe ML	33	357	340	353	SnSe ML	42	181	170	190
GeTe ML	42	—	—	308	SnTe ML	51	—	—	50

^a Ref. (Wang and Qian, 2017b). ^b Ref. (Rangel *et al.*, 2017).
^c Our calculations.

even damage ultrathin samples. STM measurements are helped by the fact that these ultrathin films are not insulators but semiconductors, such that a tunneling current can be established into the metallic substrate (Chang and Parkin, 2020).

Being a vector, \mathbf{P} has a magnitude P , an orientation, and sense of direction. SHG can only tell orientation, while two-terminal electric measurements and STM [see Figs. 2(b-e)] can determine orientation and sense of direction. These three techniques require additional calibration to uncover the magnitude (P), whose calculated values are listed in Table IV.

Similar to subplots (v) and (vi) in Fig. 2(b) showing band bending of SnTe MLs on STM topography images, SnSe ML nanoplates display the band bending seen in Fig. 3(c) as a result of bound charges accumulated at the nanoplates' edges, reflecting the in-plane polarization \mathbf{P} of these 2D ferroelectrics. The direction of \mathbf{P} for SnSe and SnTe MLs—shown by arrows with a \mathbf{P} label in Figs. 2(b) and 3(b-e)—is identified by band bending at nanoplate edges, and by the difference of lattice parameters a_1 and a_2 as extracted from atomically resolved STM images. Stripe-shaped $\sim 90^\circ$ “head-to-tail” domains are observed in SnTe monolayer plates in Fig. 3(b) (Chang *et al.*, 2016), while 180° domains are formed in SnSe MLs (Chang *et al.*, 2020). The different type of domains formed in SnSe and SnTe MLs has to do with a lattice commensuration of SnSe MLs on graphene (Chang *et al.*, 2020). A decrease of Sn vacancy concentration by 2~3 orders of magnitude was found in SnTe MLs with respect to bulk values (Chang *et al.*, 2016). Electronic band gaps of SnSe and SnTe MLs (obtained by the determination of the valence and conduction band edges *via* dI/dV measurements) are listed in Table VII.

Band bending disappears in SnTe MLs at 270 K (Chang *et al.*, 2016), but it can still be observed at 300 K in SnSe MLs, implying a robust in-plane ferroelectricity at room temperature in 2D SnSe. According to variable temperature dI/dV mapping experiments, T_c reaches 380–400 K for SnSe MLs, a promising magnitude for room-temperature applications. A theoretical description of thermally-driven structural transformations can be found in Section VII.

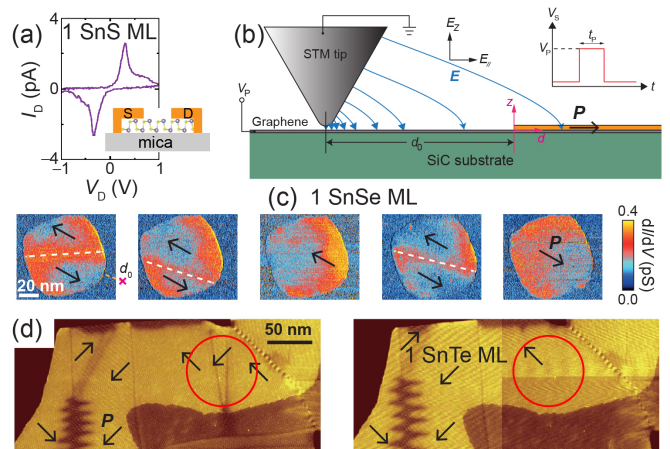


FIG. 4 (a) Ferroelectric resistive switching of a SnS ML on mica *via* source/drain bias. Taken from Ref. (Higashitaru-mizu *et al.*, 2020) under the terms of the CC-BY Attribution License. Copyright, 2020, Springer Nature. (b) Ferroelectric switching on a SnSe ML is achieved by bias voltage pulses V_P applied on the STM tip at a point on the graphene substrate close the SnSe ML plate. (c) Consecutive dI/dV images along a ferroelectric switching sequence of a SnSe ML at room temperature. The pulses were applied at the point indicated by a cross on the first panel, and white dashed lines indicate a 180° domain wall. Adapted from Ref. (Chang *et al.*, 2020) under the terms of the CC-BY Attribution License. Copyright, 2020, American Chemical Society. (d) Ferroelectric switching of a SnTe ML by an STM tip. Taken from Ref. (Chang *et al.*, 2016) with permission. Copyright, 2016, American Association for the Advancement of Science.

IV. SWITCHING THE DIRECTION OF \mathbf{P} ON O-MX MLs: DEMONSTRATING FERROELECTRIC BEHAVIOR

O-MX MLs can only be considered ferroelectrics if they can be controllably switched by an external electric field. For this purpose, a two-terminal device was built by adding silver contacts to the SnS ML grown on mica, and the current I_D was measured as the drain bias V_D was swept from -1 V to 1 V, and back to -1 V. The result, shown in Fig. 4(a), demonstrates the ferroelectric resistive switching of SnS MLs.

In addition, the domains of SnSe MLs can be switched and domain walls moved by applying bias voltage pulses onto the graphene substrate away from a SnSe nanoplate as schematically laid out in Fig. 4(b). Fig. 4(c) demonstrates the consecutive manipulation of 180° domains in a SnSe ML nanoplate. Demonstrating ferroelectric control, the polarization of the whole plate can be reversed by this approach. Statistical studies suggest a critical in-plane electric field of domain wall movement of $E_{\parallel,c} = 1.4 \times 10^5$ V/cm. Polarization switching was also demonstrated by applying bias voltage pulses to the STM tip at the surface of SnTe MLs, which locally switches ferroelectric domains by the domain wall motion highlighted within circles in Fig. 4(d).

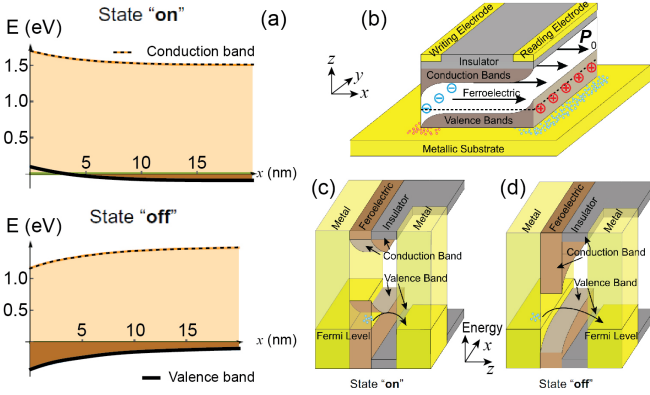


FIG. 5 (a) Schematics of upward (top) and downward (bottom) band bending near a ferroelectric’s edge, for a chemical potential near the valence band edge. The Fermi energy of the electrode was set to be $E = 0$. (b)-(d) Device schematics (b) and band diagrams for the “on” (c) and “off” (d) states. Adapted from Ref. (Shen *et al.*, 2019a). Copyright, 2019, American Physical Society.

A. Polarization switching and ultrathin memories based on in-plane ferroelectric tunnel junctions

Ferroelectrics find applications in nonvolatile memories due to their switchable bistable ground states (Scott and Paz de Araujo, 1989). First-generation ferroelectric memories use the surface charge in a ferroelectric capacitor to represent data (Evans and Womack, 1988). As a result, discharging the capacitor to measure the charge destroys the stored data, and the capacitor must be recharged after reading. A second generation of these memories probes the ferroelectric polarization using a tunneling-electroresistance effect (Tsymbal and Kohlstedt, 2006) within a metal-ferroelectric-metal junction in which an *out-of-plane* \mathbf{P} exists within the ferroelectric thin film. The tunneling potential barrier is determined by the out-of-plane polarization in the ferroelectric layer.

It may be possible to create *in-plane ferroelectric memories* by adding an insulator and a top gate to the two-terminal device shown in Fig. 4(a). Indeed, if \mathbf{P} points in-plane, such as in O-*MX* MLs, the band bending at the ferroelectric materials’ edge can be read out with metal contacts (Shen *et al.*, 2019a). As depicted by the dependency of I_D on V_D in Fig. 4(a), the upward or downward band bending drawn in Fig. 5(a) could represent the “on” or “off” state respectively, so that the information stored is read nondestructively.

Fig. 5(b) shows a ferroelectric thin film sandwiched between a metallic substrate and a wide-band-gap insulator. The writing and reading electrodes are deposited at opposite edges of the top insulator. If \mathbf{P}_0 lies in-plane along the $+x$ direction, it will induce opposite net charges at the ferroelectric boundaries along that direction. Depending on the polarization direction (either $+x$ or $-x$), the band bending near the reading electrode could be

upward or downward, leading to “on” and “off” states [Figs. 5(c) and Figs. 5(d), respectively]. Reading is non-destructive because the electric field generated by the reading voltage is perpendicular to the ferroelectric’s polarization. Using Landauer’s conductance formalism and suitably chosen parameters, currents of the order of μA and I_{on}/I_{off} ratios of the order of 10^4 have been predicted (Shen *et al.*, 2019a). See Refs. (Shen *et al.*, 2019b) and (Kwon *et al.*, 2020) for additional memory devices based on O-*MX*s.

V. LINEAR ELASTIC PROPERTIES, AUXETIC BEHAVIOR, AND PIEZOELECTRICITY OF O-*MX* MLs

The physical properties of 2D materials can be tuned by strain (Amorim *et al.*, 2016; Naumis *et al.*, 2017). In linear elasticity theory, the strain tensor is defined as $\epsilon_{ij} \simeq \frac{1}{2} \left(\frac{\partial u_i}{\partial x_j} + \frac{\partial u_j}{\partial x_i} \right)$, where $\mathbf{u} = (u_x, u_y, u_z)$ is the displacement field $\mathbf{u} = \mathbf{r} - \mathbf{r}_0$ away from a structural configuration that minimizes the structural energy.

The constitutive relation establishes a linear dependence among the stress tensor σ_{ij} and ϵ_{ij} : $\sigma_{ij} = C_{ijkl}\epsilon_{kl}$, where C_{ijkl} is the elasticity tensor. Symmetry restrictions on O-*MX* MLs imply that only C_{xxxx} , C_{xyxy} , C_{yyyy} , and C_{xyxy} are non-zero (Fei *et al.*, 2015; Gomes *et al.*, 2015); subindices xx and yy label compressive/tensile (normal) strain, and xy is a shear strain. Using Voigt notation ($xx \rightarrow 1$, $yy \rightarrow 2$, and $xy \rightarrow 6$), these entries of the elasticity tensor are commonly written as C_{11} , C_{12} , C_{22} , and C_{66} and their magnitudes are listed in Table V.

C_{11} , C_{22} , and C_{12} are obtained by fitting against the elastic energy landscape shown in Fig. 6(a), in which $\epsilon_1 = \frac{\Delta a_1}{a_{1,0}} = \frac{a_1 - a_{1,0}}{a_{1,0}}$ and $\epsilon_2 = \frac{\Delta a_2}{a_{2,0}}$. Consistent with the change in area in going from the bulk to a ML, elastic constants tend to be slightly softer in MLs than in the bulk. Ref. (Gomes *et al.*, 2015) provides the Young’s modulus for GeS, GeSe, SnS and SnSe as well, which is an order of magnitude smaller than its magnitude of 340 N/m for graphene (Lee *et al.*, 2008). Additionally, C_{11} and C_{22} are smaller when compared to their values for MoS₂ and GaSe MLs, listed in Table V as well. The shear elastic coefficient C_{66} in Table V is as small as C_{11} : shear strain changes the magnitude of $\Delta\alpha$ in Fig. 1(c), implying that distortions by such an angle are as soft as a compression or elongation along the \mathbf{a}_1 direction. In light of Table V, O-*MX* MLs are *soft* 2D materials with anisotropic elastic properties.

The Poisson’s ratio ν determines the rate of contraction in transverse directions under longitudinal uniaxial load. Most materials have a *positive* Poisson’s ratio but, as discussed in Refs. (Gomes *et al.*, 2015; Jiang and Park, 2014; Kong *et al.*, 2018; Liu *et al.*, 2019a) and summarized in Table VI, the buckled structure of O-*MX* MLs depicted in Fig. 1(c) confers them with negative ratios

TABLE V Relaxed-ion components of the elastic tensor C_{ij} for O- MX MLs in N/m. Adapted from Refs. (Gomes *et al.*, 2015) and (Fei *et al.*, 2015).

Material	\bar{Z}	C_{11}	C_{22}	C_{12}	C_{66}
GeS ML	24	15.24–20.87	45.83–53.40	21.62–22.22	18.59
GeSe ML	33	13.81–20.30	46.62–50.16	17.49–19.45	23.19
SnS ML	33	14.91–20.86	35.97–43.15	15.22–18.14	19.56
SnSe ML	42	19.61–19.88	40.86–44.49	16.36–18.57	13.70
MoS ₂ ML ^a		130	130	32	–
GaSe ML ^b		83	83	18	–

^a Ref. (Duerloo *et al.*, 2012). ^b Ref. (Li and Li, 2015).

TABLE VI Sign of Δh_0 and linear Poisson's ratio ν_{ij} of a BP ML and of O- MX MLs. Negative values of ν_{ij} indicate auxetic behavior. Adapted from Refs. (Jiang and Park, 2014; Kong *et al.*, 2018; Liu *et al.*, 2019a).

Material	\bar{Z}	Δh_0	ν_{yx}	ν_{xy}	ν_{zx}	ν_{zy}
BP	15	0	0.400	0.930	0.046	-0.027
GeS ML	24	+	0.420	1.401	-0.208	0.411
GeSe ML	33	-	0.391	1.039	0.583	-0.433
SnS ML	33	+	0.422	0.961	-0.004	0.404
SnSe ML	42	+	0.423	0.851	-0.210	0.352
SnTe ML	51	-	0.423	0.480	0.242	0.109

when the out-of-plane (z -direction) is considered. The subindices of ν_{ij} in Table VI indicate the (linear) Poisson's ratio along the i direction due to a load along the j direction as defined in Fig. 1. Negative values of ν_{ij} are indicative of *auxetic* behavior, *i.e.*, an elongation (compression) occurs along the i direction when these 2D materials are elongated (compressed) along the j direction. According to Table VI, there is a direct correlation between a positive Δh_0 in Fig. 1(a) and a negative ν_{zx} .

The third-order piezoelectric tensor d_{ijk} links $\Delta \mathbf{P} = \mathbf{P} - \mathbf{P}_0$ with the applied strain ϵ_{jk} . Using Voigt notation for the last two entries of the piezoelectric tensor and for the applied strain, Fig. 6(b) displays a ten times larger magnitude of d_{11} for GeS, GeSe, SnS, and SnSe when contrasted with the piezoelectric coefficients of quartz and other polar materials (Fei *et al.*, 2015).

VI. STRUCTURAL DEGENERACIES AND ANHARMONIC ELASTIC ENERGY OF O- MX MLs

As it turns out, the elastic energy landscape from which elastic properties were discussed in Sec. V is non-linear. Its non-linearity underpins the highly anharmonic vibrational properties and a propensity of O- MX MLs for sudden changes in ferroelectric, structural, electronic, spin, and optical properties with temperature.

Turning the $\Delta a_1/a_{1,0} = (a_1 - a_{1,0})/a_{1,0}$ axis in Fig. 6(a) into a_1 and $\Delta a_2/a_{2,0}$ into a_2 , and increasing the range for both a_1 and a_2 from which the structural energy $E(a_1, a_2)$ is computed, the elastic energy landscape $\Delta E(\epsilon_1, \epsilon_2) = \Delta E(a_1, a_2) = E(a_1, a_2) -$

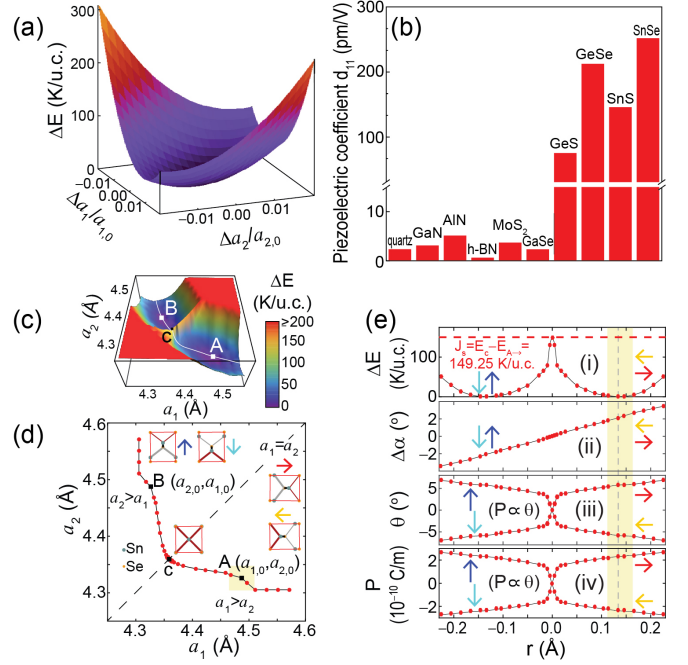


FIG. 6 (a) Elastic energy landscape of a SnSe ML (in units of K/u.c.) as a function of uniaxial strain along the a_1 and a_2 directions. Adapted from Ref. (Gomes *et al.*, 2015) with permission. Copyright, 2015, American Physical Society. (b) Piezoelectric coefficient d_{11} of GeS, GeSe, SnS and SnSe MLs and other known piezoelectric materials. Adapted from Ref. (Fei *et al.*, 2015) with permission. Copyright, 2015, American Institute of Physics. (c) Elastic energy landscape over a larger range of values for a_1 and a_2 ; point A corresponds to the ground state unit cell shown in Fig. 1(c). (d) Two-dimensional lowest-energy path joining degenerate ground states A and B; the shaded rectangle corresponds to $\pm 0.5\%$ strain. (e) Change in energy ΔE , $\Delta\alpha$, θ , and P in going through the path shown in (c); the dashed vertical line cuts through $\Delta E = 0$ and thus shows $\Delta\alpha_0$, θ_0 and P_0 . Subplots (c-e) are adapted from Ref. (Barraza-Lopez *et al.*, 2018) with permission. Copyright, 2018, American Physical Society.

$E(a_{1,0}, a_{2,0})$ shown in Fig. 6(c) ensues. Given that $E(a_{1,0}, a_{2,0}) = E(a_{2,0}, a_{1,0})$ on 2D materials with a rectangular u.c. ($a_{1,0} > a_{2,0}$), the elastic energy landscape has two degenerate structures labeled A and B in Fig. 6(c) (Mehboudi *et al.*, 2016a; Wang and Qian, 2017b). O- MX s have eight degenerate u.c.s, occurring upon a mirror reflection with respect to the $x-z$ or $x-y$ planes, or by an exchange of $x-$ and $y-$ coordinates (Mehboudi *et al.*, 2016a). Nevertheless, an inversion with respect to the $x-y$ plane does not change the orientation nor the sense of direction of \mathbf{P}_0 and is usually disregarded when describing degeneracies for that reason; the four remaining degenerate ground state u.c.s are displayed as an inset in Fig. 6(d). They have projections $\mathbf{p}_0 \rightarrow, \uparrow, \leftarrow,$ and \downarrow that are reminiscent of discrete clock models—well known tools to discuss order-by-disorder 2D transformations in Statistical Mechanics (Potts, 1952) that provide

important insight into the finite temperature behavior of O–MX MLs (Mehboudi *et al.*, 2016a).

The saddle point c in Fig. 6 indicates the minimum elastic energy necessary to switch in between ferroelectric states A and B . It is situated at (a_c, a_c) , with $a_c = \left(1 - \frac{1}{\sqrt{2}}\right)a_{1,0} + \frac{a_{2,0}}{\sqrt{2}}$ (Poudel *et al.*, 2019). The five-fold coordinated u.c. at point c is paraelectric (Mehboudi *et al.*, 2016a) and it belongs to symmetry group 129 ($P4/nmm$, or $Pmm4/n$ with our choice of axes) (Vilanova *et al.*, 2020). J_s is the energy difference in between the five-fold coordinated paraelectric u.c. at point c and any of the degenerate ferroelectric ground states (*i.e.*, the one at point A with polarization along the positive x -direction): $J_s = E_c - E_{A \rightarrow} = E(a_c, a_c) - E(a_{1,0}, a_{2,0})$. J_s indicates the ease of a ferroelastic transformation among a pair of degenerate structures shown in Fig. 6(d). As it will be discussed in Sec. VII, it is a qualitative estimator of the critical temperature T_c at which a ferroelectric to paraelectric transition takes place in these 2D materials. [$a_{1,0} = a_{2,0} = a_c$ for PbX MLs in Fig. 1(d), which hence have a single non-degenerate structural ground state and $J_s = 0$.]

The white path $r(a_1, a_2)$ in Fig. 6(c) provides the lowest-energy distortion that is necessary to turn degenerate structure A into B elastically, and it is projected into a 2D plot in Fig. 6(d). For a SnSe ML, points A and B are located at distances $r = 0.134 \text{ \AA}$ and $r = -0.134 \text{ \AA}$ along this path; point c is located at $r = 0 \text{ \AA}$. The range of values utilized to extract linear elastic properties in Sec. V can be seen as a yellow (light gray) rectangle in Fig. 6(d).

The anharmonicity of the elastic energy landscape is established by the double-well potential $\Delta E(r)$ seen as subplot (i) in Fig. 6(e). The magnitude of J_s for a SnSe ML [as computed with the vdW-DF-cx (Berland and Hyldgaard, 2014) XC functional] can also be seen in that plot. The dependency of ΔE on the path coordinate r is *bistable* (*i.e.*, fundamentally non-harmonic). The evolution of $\Delta\alpha$, θ , and the polarization P along r —including the four possible orientations of \mathbf{p} (\mathbf{P})—is displayed as subplots (ii), (iii), and (iv) in Fig. 6(e). The area in yellow (light gray) on Fig. 6(e) corresponds to the $\pm 0.5\%$ strain within which ΔE can be fitted to a parabola, and where $\Delta\alpha$, θ , and P are linear on r .

The vertical dashed line, crossing through $\Delta E = 0$ shows $\Delta\alpha_0$, θ_0 , and P_0 ; *i.e.*, the magnitudes of these variables in a u. c. like the one seen in Fig. 1(c). The angle $\Delta\alpha$ is positive for $r > 0$ ($a_1 > a_2$), zero at $r = 0$ ($a_1 = a_2$), and negative for $r < 0$ ($a_1 < a_2$). The angle θ , in turn, points along the (positive or negative) x -direction when $r > 0$, it is zero at $r = 0$, and it points along $\pm y$ when $r < 0$. Importantly, θ and P are linearly proportional ($P \propto \theta$) and $P = 0$ when $\theta = 0$ and $\Delta\alpha = 0$ in an elastic transformation in which lattice parameters can vary. The possibility of switching \mathbf{P}

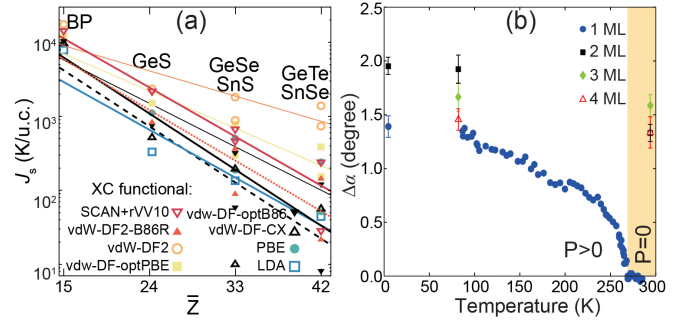


FIG. 7 (a) Exponential dependency of J_s on \bar{Z} . This plot also shows the dependence of J_s (and therefore of $a_{1,0}$, $a_{2,0}$, $\Delta\alpha_0$, P_0 , and θ_0) on the XC functional employed. Taken from Ref. (Poudel *et al.*, 2019) with permission. Copyright, 2019, American Physical Society. (b) Experimental thermal dependency of $\Delta\alpha$ for few-layer SnTe on epitaxial graphene. A paraelectric phase ($P=0$) ensues at temperatures above $T_c = 270$ K in SnTe MLs. Adapted from Ref. (Chang *et al.*, 2016) with permission. Copyright, 2016, American Association for the Advancement of Science.

gives rise to a combined ferroelectricity and ferroelasticity; *i.e.*, to multiferroic behavior in O–MX MLs (Wang and Qian, 2017b; Wu and Zeng, 2016).

VII. STRUCTURAL PHASE TRANSITION AND PYROELECTRIC BEHAVIOR OF O–MX MLs

Structural degeneracies underpin strong anharmonic elastic properties, soft phonon modes, and structural phase transitions. Taking J_s —the relevant energy scale in the system—as an *ad-hoc* exchange parameter, a clock model with $r = 4$ degenerate states yields the following relation among T_c and J_s : $T_c = 1.136J_s$ (Potts, 1952). The Potts model also has a prescription in case that only a subset of two degenerate states is available (*e.g.*, \rightarrow and \leftarrow), which could occur in a constrained scenario in which a_1 and a_2 keep zero-temperature magnitudes (Fei *et al.*, 2016): calling J_r the energy barrier under such constrained configuration, Potts dictates that $T'_c = 2.272J_r$ (Potts, 1952). Numerical calculations indicate that $J_r \geq 1.4J_s$, so that $T'_c \geq 2.8T_c$. The message is that structural constraints lead to an increased T_c .

The ferroelectric-to-paraelectric transition temperature T_c of O–MX MLs calculated at the DFT level (Martin, 2004) has a strong dependency on the choice of XC functional, and it is unclear that the PBE XC functional ought to provide the most accurate description of the thermal behavior of O–MXs. The strong dependency of T_c on XC functional can be already foreseen in the magnitude of J_s displayed in Fig. 7(a), which contains predictions with LDA, PBE, multiple non-empirical van der Waals implementations (Berland *et al.*, 2015), and even the recent SCAN+rVV10 (Peng *et al.*, 2016) XC functional (Poudel *et al.*, 2019).

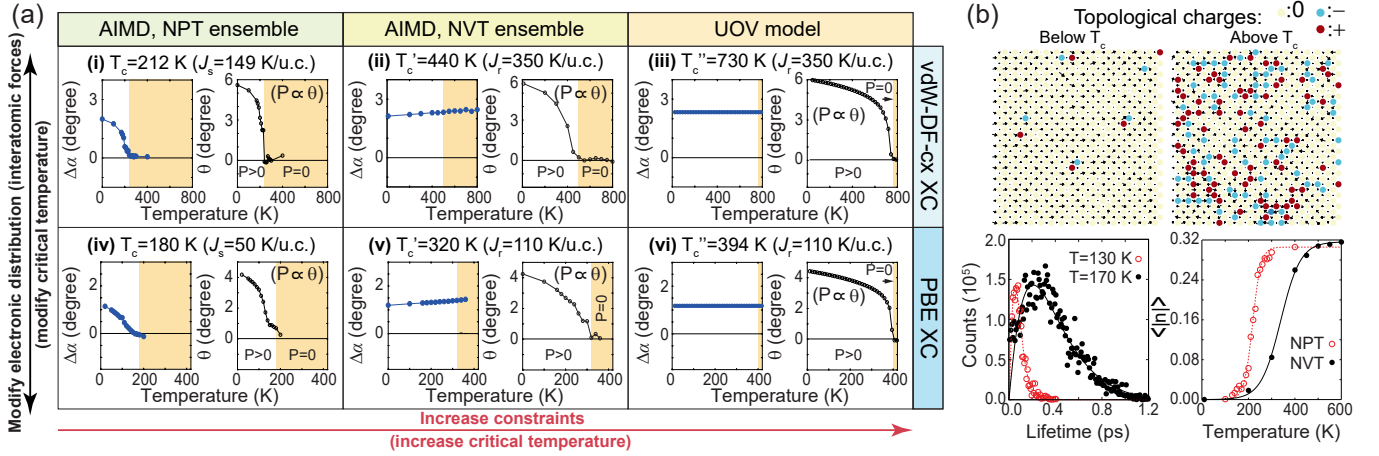


FIG. 8 (a) Temperature dependence of $\Delta\alpha$ and θ for a SnSe ML in AIMD calculations employing two XC functionals, and obtained within the NPT [subplots(i) and (iv)] and NVT ensembles [subplots(ii) and (v)]. Results from the more constrained unidirectional optical vibration (UOV) model are presented in subplots (iii) and (vi). The ferroelectric phase occurs when $\theta > 0$. Note that $\Delta\alpha = 0$ implies $\theta = 0$ but that $\theta = 0$ does not necessarily imply $\Delta\alpha = 0$. (b) The structural transformations described by AIMD can be understood in terms of a fluctuating connectivity (*i.e.*, topology) of these 2D ferroelectrics. Pairs of topological charges have a temperature-dependent lifetime and their number saturates at temperatures within T_c . Results in (b) were obtained using the vdW-DF-cx functional. Adapted from Ref. (Villanova *et al.*, 2020) with permission. Copyright, 2020, American Physical Society.

Ab initio molecular dynamics (AIMD) calculations performed on freestanding SnSe MLs using the NPT ensemble (in which containing walls are allowed to move to accommodate for thermal expansion) provide the following information: (i) T_c is larger in GeSe MLs and bilayers than it is in SnSe MLs and bilayers, owing to the smaller \bar{Z} and hence larger barrier J_s [Fig. 7(a)] for GeSe; (ii) for a given O-MX, T_c increases with increasing number of MLs (Chang *et al.*, 2016; Mehboudi *et al.*, 2016b). A slight dependency of T_c in the size of the simulation supercell has been documented, too (Barraza-Lopez *et al.*, 2018; Mehboudi *et al.*, 2016b). In agreement with J_s 's inverse dependency on \bar{Z} , experiments indicate a T_c larger than 400 K for SnSe ($\bar{Z} = 42$) on graphene (Chang *et al.*, 2020), and $T_c = 270$ K for SnTe MLs ($\bar{Z} = 51$) on the same substrate [Fig. 7(b) (Chang *et al.*, 2016)].

The upper row in Fig. 8(a) shows a progression of T_c estimates for a freestanding SnSe ML that were obtained using the vdW-DF-cx XC functional (Berland and Hyldgaard, 2014). From left to right, the figure displays the thermal behavior of $\Delta\alpha$ and θ when (i) using the NPT ensemble (in which containing walls move so that the material remains at atmospheric pressure), (ii) the NVT ensemble (in which the supercell volume V is fixed and containing walls do not move), and (iii) a unidirectional optical vibration (UOV) model in which only one vibrational mode—out of twelve—is employed and the containing walls do not move either (Fei *et al.*, 2016). The point is that (as already foreseen by the Potts model a few lines above) T_c increases with added constraints. Energy barriers J_s and J_r are listed in that Figure, too.

Briefly said, AIMD calculations carried out with the

NPT ensemble yield the smallest magnitude of T_c (212 K). Although the compounds are not the same (a freestanding SnSe ML in calculations and a SnTe ML on graphene in experiment), the decay of $\Delta\alpha$ in the calculations seen in subplot (i) of Fig. 8(a) indicates a phenomenology consistent with experiment in Fig. 7(b) (Barraza-Lopez *et al.*, 2018; Chang *et al.*, 2016). When constraining the SnSe ML by not permitting its area to increase at finite temperature, the structural transition within the NVT ensemble necessarily requires additional (thermal) energy to take place, raising T_c' up to 440 K and displaying $\Delta\alpha > 0$ at T_c . Despite the existence of nearly degenerate vibrational modes oscillating along both x - and y -directions, the highly constrained UOV model only permits an optical vibration along the x -direction (an oscillatory mode valid only at the Γ -point) and thus yields the largest $T_c'' = 730$ K, still showing $\Delta\alpha > 0$ at T_c as a_1 and a_2 are kept fixed [Eqn. (1)]. $\Delta\alpha$ [Fig. 7(b)] is not a relevant order parameter for subplots (ii) and (iii) in Fig. 8(a) because a_1 and a_2 retain their zero-temperature values in these models.

The increasing sequence of critical temperatures observed with increasing mechanical constraints is independent of the XC approximation, as the lower row in Fig. 8(a) shows a similar phenomenology when the PBE XC functional is employed. T_c , T_c' , and T_c'' have smaller values than those obtained with the vdW-DF-cx XC functional (Villanova *et al.*, 2020). As illustrated in Fig. 8(b), the structural transition is underpinned by changes in the connectivity of the 2D lattice as the two atoms defining the angle θ in Fig. 1(a) rotate about the out-of-plane z -axis; this change in connectivity confers

a topological character to the structural transformation (Kosterlitz, 2016; Villanova *et al.*, 2020; Xu *et al.*, 2020).

Pyroelectricity is the creation of electricity by a temperature gradient. Given the direct proportionality between θ and P , the temperature derivative of θ in Fig. 8(a) gives a direct insight into the pyroelectric properties of O- MX s (Mehboudi *et al.*, 2016b).

The effects of substrates such as Ni, Pd, Pt, Si, Ge, CaO, and MgO on the morphology and properties of SnTe MLs (including charge transfer and atomistic distortions) have been studied (Fu *et al.*, 2019). Since O- MX MLs are presently grown on substrates, the effect of the substrate- MX interaction on the transition temperature is an important avenue for further theory. Along these lines, the elastic energy barriers J_s of GeSe, GeTe, SnS, SnSe, and SnTe have been shown to vanish under a modest hole doping of 0.2 $|e|/\text{u.c.}$, where e is the electron's charge (Du *et al.*, 2020; Zhu *et al.*, 2020).

We indicated in Sec. II that O- MX s are isostructural to BP. This makes BP MLs doubly-degenerate upon exchange of x - and y - coordinates, and suggests that BP MLs may also undergo a phase transition at finite temperature. Nevertheless, considering J_s as an approximate measure of T_c , one observes $J_s > 1,000$ K/u.c. for BP in Fig. 7(a) regardless of XC functional. Such magnitude is so large that a BP ML melts rather than undergoing a ferroelastic to paraelastic transition (Mehboudi *et al.*, 2016a), thus explaining the lack of *thermally-driven* 2D phase transitions in BP MLs. [BP MLs have been shown to undergo temperature-independent 2D phase transitions by mechanical strain (Rodin *et al.*, 2014b).] The propensity to undergo thermally-driven 2D transitions is a crucial aspect that sets O- MX MLs apart from other 2D materials such as graphene, TMDC MLs with a 2H symmetry, and BP MLs.

VIII. ELECTRONIC, VALLEY AND SPIN PROPERTIES OF O- MX MLs

A. Electronic band structure

TMDC MLs such as 2H-MoS₂ display an indirect-to-direct band gap crossover at the ML limit. As indicated in Table VII, the experimental band gap of MoS₂ increases from 1.29 eV in the bulk up to 1.90 eV in a ML due to quantum confinement (Mak *et al.*, 2010), and the valence band maxima (VBM) and conduction band minima (CBM) are both located at the high-symmetry $\pm\mathbf{K}$ -points in these MLs. Similarly, quantum confinement leads to an increase of the electronic band gap of BP (Table VII), and its electronic bands are highly anisotropic. The VBM and CBM are both located at the Γ -point in BP MLs (Tran *et al.*, 2014).

Tritsaris, Malone, and Kaxiras (Tritsaris *et al.*, 2013) studied the electronic properties of SnS down to the ML

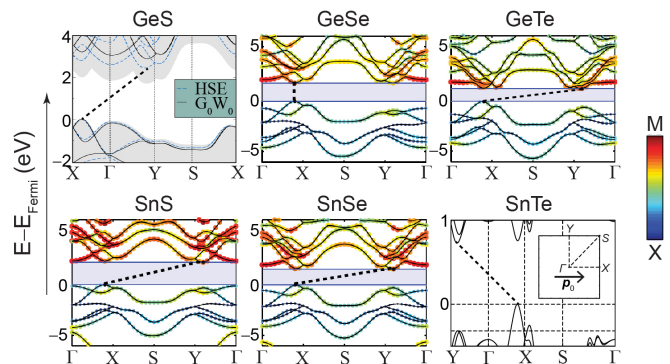


FIG. 9 Electronic band structure of O- MX MLs. With the exception of the SnTe ML, these calculations were carried out with the HSE06 XC functional. GeSe MLs have direct band gaps, and the GeTe ML subplot was modified to account for an indirect band gap smaller by just 0.01 eV than the direct band gap. The inset in the SnTe subplot displays the high-symmetry points and the direction of \mathbf{p}_0 . Adapted from Ref. (Singh and Hennig, 2014) with permission. Copyright, 2014, American Institute of Physics. The GeS subplot was taken from Ref. (Gomes *et al.*, 2016) with permission. Copyright, 2016, American Physical Society. The SnTe subplot was adapted from Ref. (Chang *et al.*, 2019b) with permission. Copyright, 2019, American Physical Society.

limit. As indicated in Table VII, the electronic band gap increases as these materials are thinned down, too. Nevertheless (and unlike the case for 2H-TMDs and BP MLs), the VBM and CBM are not located at high-symmetry points in the first Brillouin zone (BZ).

With reciprocal lattice vectors $\mathbf{b}_1 = \frac{2\pi}{a_{1,0}}(1, 0, 0)$ and $\mathbf{b}_2 = \frac{2\pi}{a_{2,0}}(0, 1, 0)$, the high-symmetry points depicted as an inset within the SnTe subplot in Fig. 9 are Γ , X (located at $\mathbf{b}_1/2$), Y (at $\mathbf{b}_2/2$), and S (at $\mathbf{b}_1/2 + \mathbf{b}_2/2$). O- MX MLs have their VBM away from high-symmetry points, at about $\pm(0.74-0.84)X$ and their CBM at about $\pm(0.74-0.84)Y$ for an indirect band gap. The exception is GeSe, having a CBM at $\pm 0.80X$ and a direct band gap (Gomes and Carvalho, 2015; Gomes *et al.*, 2016; Shi and Kioupakis, 2015; Singh and Hennig, 2014). Electronic band structure calculations within the GW approximation (Deslippe *et al.*, 2012) were carried out in Refs. (Shi and Kioupakis, 2015; Tuttle *et al.*, 2015) and (Gomes *et al.*, 2016); their band gaps are listed in Table VII. The electronic band structure of O- MX s turns more (less) anisotropic for lighter (heavier) compounds, for which $a_{1,0}/a_{2,0}$ in Fig. 1(d) takes on larger (smaller) values. Going across chemical elements, the band gap for O- MX MLs in Table VII is tunable with \bar{Z} : it takes its largest magnitude for lighter compounds (GeS, $\bar{Z} = 24$) and it is smaller for the heaviest compound (SnTe, $\bar{Z} = 51$).

From an experimental perspective, hole-doped SnTe MLs acquire a domain structure observed as dark vertical lines in Figs. 3(b) and 10(a). As seen in Figs. 10(b) and

TABLE VII Electronic band gap (in eV) for BP, O–MXs and MoS₂ (ML and bulk) with PBE and HSE XC functionals (Heyd *et al.*, 2003), from GW calculations (Deslippe *et al.*, 2012), or experiment. PBE values for GeTe and SnTe MLs, and for bulk SnTe were computed by us.

Material	\bar{z}	PBE (ML)	HSE (ML)	GW (ML)	Exp. (ML)	PBE (bulk)	HSE (bulk)	Exp. (bulk)
BP	15	0.90 ^a	1.66 ^a	2.2 ^b		0.07 ^a	0.39 ^a	0.33 ^c
GeS	24	1.65 ^a	2.32 ^a	2.85 ^d		1.22 ^a	1.81 ^a	1.70-1.96 ^e
GeSe	33	1.18 ^a	1.54 ^a	1.70-1.87 ^{d,f}		0.57 ^a	1.07 ^a	1.14 ^g
GeTe	42	0.87				0.33 ^h	0.65 ^h	0.61 ⁱ
SnS	33	1.38 ^a	1.96 ^a			0.82 ^a	1.24 ^a	1.20-1.37 ^e
SnSe	42	0.96 ^a	1.44 ^a	1.63 ^f	2.1 ^j	0.54 ^a	1.00 ^a	0.90 ^k
SnTe	51	0.68			1.6 ^l	0.13		0.30 ^m
MoS ₂	–	1.63 ⁿ	2.11 ⁿ		1.90 ^o	0.98 ⁿ	1.46 ⁿ	1.29 ^o

^a Ref. (Gomes and Carvalho, 2015). ^b Ref. (Wang *et al.*, 2015). ^c Ref. (Keyes, 1953). ^d Ref. (Gomes *et al.*, 2016).

^e Ref. (Malone and Kaxiras, 2013). ^f Ref. (Shi and Kioupakis, 2015). ^g Ref. (Vaughn *et al.*, 2010).

^h Ref. (Di Sante *et al.*, 2013). ⁱ Ref. (Park *et al.*, 2009).

^j Ref. (Chang *et al.*, 2020). ^k Ref. (Parenteau and Carlone, 1990). ^l Ref. (Chang *et al.*, 2016). ^m Ref. (Dimmock *et al.*, 1966). ⁿ Ref. (Shi *et al.*, 2017). ^o Ref. (Mak *et al.*, 2010).

10(d), the spatially resolved dI/dV spectra [proportional to the sample’s local density of states (LDOS)] features electronic standing wave patterns across domains for energies below the VBM that provide indirect information into these materials’ electronic properties.

The standing wave patterns observed at 4 K are induced by the electronic band mismatch at the two sides of a 90° domain wall [see domains with \mathbf{P} forming $\sim 90^\circ$ angles in Figs. 2(b) and 3(b)]. As Fig. 10(c) shows, the band apexes along the $\Gamma - Y$ direction are 0.3 eV below those seen along the $\Gamma - X$ direction. Such mismatch of hole momentum prevents a direct (elastic, unscattered) transmission of holes through domain walls, giving rise to a peculiar reflection resulting in standing waves (Chang *et al.*, 2019b).

In fact, and as depicted in Fig. 10(c), the reflection off a domain wall occurs *via* a momentum transfer \mathbf{q} occurring within each hole band. This observation implies that the standing wave pattern is an indirect measure of the electronic band structure around the VBM. From the Fourier transform of the standing wave pattern in Fig. 10(d), a single branch of the energy dispersion with scattering vector q [inset in Fig. 10(c)] is experimentally resolved in Fig. 10(e) (Chang *et al.*, 2019b); note that $P(T = 4K) \simeq P_0$. Although spin-orbit interaction induces band splitting at the VBM, the contribution from the two spin components to the standing wave pattern are identical because of time reversal symmetry.

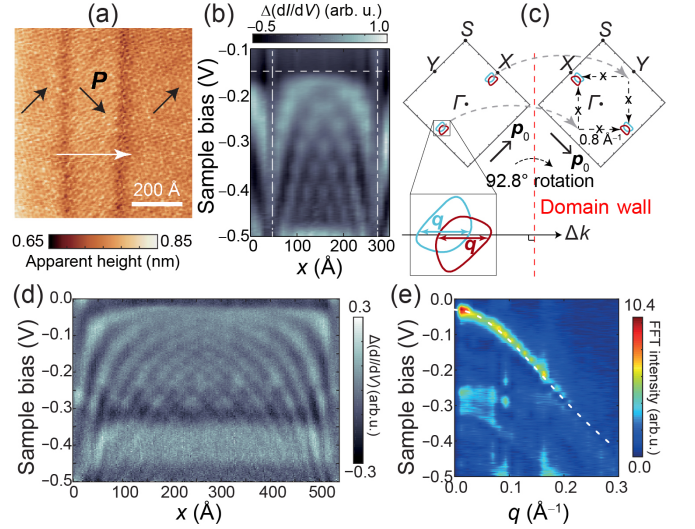


FIG. 10 (a) STM topographic image of $\sim 90^\circ$ domains on a SnTe ML. (b) dI/dV spectra acquired along the white arrow in (a) at energies around the VBM. (c) Mismatched hole bands at opposite sides of a 90° domain wall. Constant energy contours with opposite spin components are colored in blue (light gray) or red (dark gray), respectively. (d) Electronic standing wave pattern across a 540 Å wide domain. (e) The Fourier transform of (d) reveals the energy dispersion of scattering vectors. The dashed white curve is the $E(q)$ dispersion as obtained from the electronic band structure. Adapted from Ref. (Chang *et al.*, 2019b) with permission. Copyright, 2019, American Physical Society.

B. Valleytronics

The band curvature \hbar^2/m^* at the VBM and CBM—where m^* is the effective mass—is used to estimate the hole and electron conductivities of semiconductors. When determined along orthogonal (x - and y -) directions, it provides information about the anisotropy of the charge carriers’ conductivity. The effective masses at the VBM ($m^* = m_h$) and CBM ($m^* = m_e$) for multiple O–MX MLs (expressed in terms of the electron’s mass m_0) are listed in Table VIII (Gomes *et al.*, 2016). With the exception of GeS MLs, these effective masses are smaller to those of MoS₂ [which range within $-(0.44-0.48)m_0$ for holes and $0.34-0.38m_0$ for electrons (Cheiwchanchamnangij and Lambrecht, 2012; Peelaers and Van de Walle, 2012)], implying sharper hole/electron pockets at the VBM/CBM on O–MX MLs than those existing in more traditional materials for valleytronic applications (Schaibley *et al.*, 2016). Such sharpness of the valence (conduction) band curvature permits stating that holes (electrons) belong to a given *valley*.

Valleytronics refers to the use of the electron/hole pockets at the CBM or VBM as information carriers (Schaibley *et al.*, 2016), which requires creating valley-specific gradients of charge carriers; *i.e.*, a *valley polarization*. Achieving valley polarization requires lifting

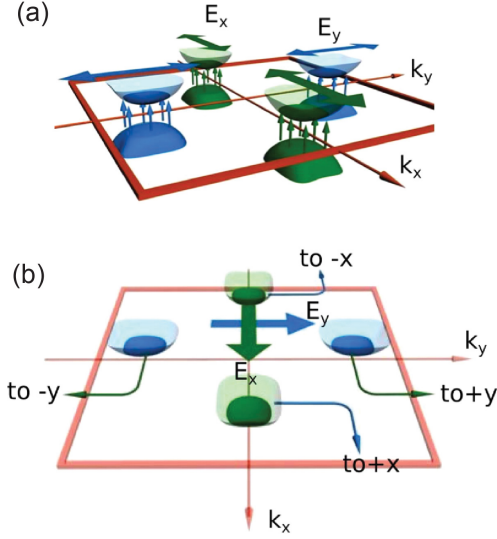


FIG. 11 (a) Valley selection under an external oscillating electric field. Different valleys are excited depending on the field’s linear polarization. (b) Valley separation under a static electric field. Depending on the polarization of the field, different valleys flow along perpendicular directions. Taken from Ref. (Rodin *et al.*, 2016) with permission. Copyright, 2016, American Physical Society.

the valley degeneracy; something that has been demonstrated in TMDC MLs (Rycerz *et al.*, 2007; Xiao *et al.*, 2012). In these 2D materials, valleys at time-reversed states $+\mathbf{K}$ and $-\mathbf{K}$ in the BZ couple to the circular polarization of light so that a pseudospin (“up” or “down”) quantum number can be associated with each valley. Valley polarization occurs because right-hand polarized photons only excite the carriers in $+\mathbf{K}$ valley, and left-hand polarized photons only excite those in $-\mathbf{K}$ valley (Cao *et al.*, 2012; Mak *et al.*, 2012; Sallen *et al.*, 2012; Zeng *et al.*, 2012). When an in-plane electric field is applied across graphene bilayers or TMDC MLs, carriers with “up” and “down” pseudospins acquire a transverse velocity in opposite directions because of the opposite Berry curvature in $+\mathbf{K}$ and $-\mathbf{K}$ valleys, giving rise to a valley Hall effect (Mak *et al.*, 2014; Shimazaki *et al.*, 2015; Sui *et al.*, 2015).

Unlike a BP ML, which has a single valley centered around the Γ -point, the sharp band curvature of the VBM and CBM of O-*MX* MLs listed in Table VIII permits considering them two-valley materials, too. They feature a valley along the $\Gamma - X$ direction (the V_x valley), and another valley along the $\Gamma - Y$ direction (V_y valley) (Rodin *et al.*, 2016), and valley-selective optical excitation can be realized in these 2D materials using linearly polarized light (Hanakata *et al.*, 2016; Rodin *et al.*, 2016; Shen *et al.*, 2017; Xu *et al.*, 2017).

Figure 11(a) shows valleys located along the $\Gamma - X$ and $\Gamma - Y$ lines in the BZ. First-principles calculations and symmetry analysis show that x -polarized photons have

TABLE VIII Anisotropic effective masses of holes (m_h/m_0) and electrons (m_e/m_0) at VBM and CBM along the x and y -directions as shown in Fig. 1(c) for O-*MX* MLs.

Material	Z	$(m_h/m_0)_x$	$(m_h/m_0)_y$	$(m_e/m_0)_x$	$(m_e/m_0)_y$
GeS ML	24	-0.26	-0.94	0.24	0.57
GeSe ML	33	-0.17	-0.32	0.17	0.34
GeTe ML	42	-0.15	-0.16	0.08	0.32
SnS ML	33	-0.24	-0.27	0.20	0.22
SnSe ML	42	-0.14	-0.14	0.14	0.14
SnTe ML	51	-0.10	-0.05	0.13	0.14

a much higher probability to excite carriers in the V_x valley. Similarly, carriers in the V_y valley can be readily excited by y -polarized light almost exclusively. In other words, a specific valley can be selectively excited by controlling the polarization of the incident light [this mechanism does not distinguish sign: for instance, both $-(\Gamma - X)$ and $+(\Gamma - X)$ are both “the V_x valley”]. As an alternative mechanism to produce valley polarization by means of time-reversal symmetry, an in-plane static electric field makes carriers excited from the V_x valley [either located along the $-(\Gamma - X)$ or $+(\Gamma - X)$ line] bend in opposite directions, generating a valley Hall effect illustrated in Fig. 11(b). A similar effect occurs when exciting the V_y valley. Additional transport effects arising from non-linear electric fields will be discussed in Sec. IX.D.

C. Persistent spin helix behavior

So far, we have considered the electronic properties of O-*MX* MLs without concern for spin polarization. Spin-orbit coupling can create various types of spin splitting near the band edges, as well as spin Hall effects in O-*MX* MLs (Sławińska *et al.*, 2019). Zeeman-like spin splitting is the prominent mechanism in TMDCs (Xiao *et al.*, 2012). On the other hand, a Rashba-like spin orbit coupling occurs in O-*MX* MLs due to the spin-orbit field $\vec{\Sigma}_{SOF}(\mathbf{k}) = \alpha(\hat{\mathbf{P}}_0 \times \mathbf{k})$, where α is the spin-orbit coupling strength, $\hat{\mathbf{P}}_0 = \mathbf{P}_0/P_0$ is the direction of the intrinsic electric polarization in ferroelectrics, and \mathbf{k} is the quasiparticle (electron or hole) crystal momentum [Fig. 12(a)].

As indicated in Sec. II, the out-of-plane component of \mathbf{P}_0 is quenched in ultrathin SnTe, making $\mathbf{P}_0 = P_0\hat{x}$. Since 2D materials lack crystal momentum along the z -direction, $\vec{\Sigma}_{SOF}(\mathbf{k}) \propto (\hat{x} \times \mathbf{k})$, with $\mathbf{k} = (k_x, k_y, 0)$. Note that spin becomes degenerate along the $\Gamma - X$ ($k_y = 0$) high symmetry line, that it points along the z -direction for $k_y \neq 0$, and it reverts direction when either k_y or \mathbf{P}_0 change sign (Lee *et al.*, 2020). Rotating \mathbf{P}_0 into the y -direction [see Fig. 6(d)] changes the orientation of the spin-split bands. The strength of the spin-orbit coupling increases with atomic number Z , as widely reported for O-*MX* MLs (Chang *et al.*, 2019b; Liu *et al.*,

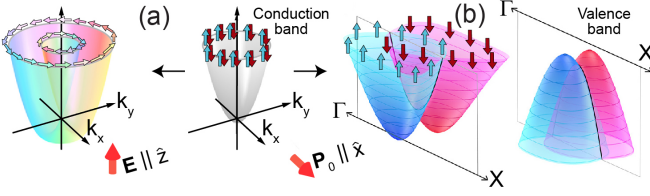


FIG. 12 (a) Conventional and (b) out-of-plane spin Rashba effects at the bottom of the conduction band. In subplot (b), the out-of-plane spin Rashba effect is realized in a SnTe ML, and both the valence and conduction bands are shown. Adapted from Ref. (Lee *et al.*, 2020) with permission. Copyright, 2020. American Institute of Physics.

2019b; Rodin *et al.*, 2016; Shi and Kioupakis, 2015) and other 2D ferroelectrics (Ai *et al.*, 2019; Di Sante *et al.*, 2015; Kou *et al.*, 2018; Wang *et al.*, 2018b). Recalling that Pb-based MX MLs lack an intrinsic polarization [$a_{1,0} = a_{2,0}$ in Fig. 1(d) and hence $\mathbf{P}_0 = 0$], the best immediate candidates for 2D ferroelectric Rashba semiconductors within MX MLs are tellurides GeTe and SnTe.

Space group $P2_1mn$ has the following symmetries: (i) the identity E ; (ii) \tilde{C}_{2x} : a two-fold rotation around the x -axis (C_{2x}), followed by a translation $\tau = (\mathbf{a}_1 + \mathbf{a}_2)/2$; (iii) a glide-reflection plane \bar{M}_{xy} : a reflection by the xy plane followed by τ ; and (iv) a reflection about the xz plane (M_{xz}) (Rodin *et al.*, 2016). Adding time-reversal symmetry as customarily defined $\hat{T} = i\sigma_y K$ (where K represents complex conjugation) the following effective spin Hamiltonian applies at the top of the valence band and at the bottom of the conduction band (Absor and Ishii, 2019; Lee *et al.*, 2020):

$$\hat{H} = \frac{\hbar^2}{2m^*} (k_x^2 + k_y^2) + (\alpha k_y + \alpha' k_x^2 k_y + \alpha'' k_y^3) \sigma_z, \quad (2)$$

with m^* , α , α' , and α'' to be fitted from band structure calculations [Fig. 12(b)]. This Hamiltonian does not have contributions from in-plane spin components up to third order in momentum, leading to a persistent spin Helix effect with a tunable *out-of-plane spin*. Eqn. (2) is similar to a Dresselhaus model for a bulk zinc blende crystal oriented along the [110] direction (Dresselhaus, 1955). Estimates of the spin-orbit coupling α in $O-MX$ s are two to three orders of magnitude larger than those in III-V semiconductor quantum well structures (Lee *et al.*, 2020), and the wavelength of their spin polarization λ is smaller than that obtained for other Rashba semiconductors (Absor and Ishii, 2019) which permits smaller lateral device dimensions: $O-MX$ MLs furnish an ideal platform for persistent spin helix dynamics (Bernevig *et al.*, 2006) in two dimensions.

SnTe ML spin transistors may be designed to have a channel length of $\lambda/4$, so that they can be electrically switched in the ferroelectric channel, or magnetically switched in the ferromagnetic drain (Lee *et al.*, 2020). Another proposal is an all-in-one spin transistor based

TABLE IX Transformation rules for k_x , k_y , σ_x , σ_y , and σ_z under the symmetry operations of group $P2_1mn$, defined as $\tilde{C}_{2x} = i\sigma_x$, $\hat{M}_{xz} = i\sigma_y$, and $\hat{M}_{xy} = i\sigma_z$. Adapted from Ref. (Absor and Ishii, 2019) to reflect the choice of lattice vectors used in this work.

Symmetry operation	(k_x, k_y)	$(\sigma_x, \sigma_y, \sigma_z)$
\hat{E}	(k_x, k_y)	$(\sigma_x, \sigma_y, \sigma_z)$
$\tilde{C}_{2x} = i\sigma_x$	$(k_x, -k_y)$	$(\sigma_x, -\sigma_y, -\sigma_z)$
$\hat{M}_{xz} = i\sigma_y$	$(k_x, -k_y)$	$(-\sigma_x, \sigma_y, -\sigma_z)$
$\hat{M}_{xy} = i\sigma_z$	(k_x, k_y)	$(-\sigma_x, -\sigma_y, \sigma_z)$
$\hat{T} = i\sigma_y K$	$(-k_x, -k_y)$	$(-\sigma_x, -\sigma_y, -\sigma_z)$

on the spin Hall effect, where the inverse spin Hall effect charge current is detuned by an out-of-plane electric field which [according to Fig. 12(a)] breaks the persistent spin helix state down and induces spin decoherence (Slawinska *et al.*, 2019).

IX. OPTICAL PROPERTIES OF $O-MX$ MLs

A. Optical absorption

Optical absorption reflects the anisotropy of the electronic band structure of $O-MX$ MLs: linearly polarized light with polarization parallel to the x -direction leads to a smaller absorption energy gap when contrasted with light whose polarization is parallel to the y -axis (Gomes and Carvalho, 2015) [this effect can be observed in Fig. 16, where GW corrections and Bethe-Salpeter electron-hole interactions have been added]. The symmetry imposed by the $P4/nmm$ structural transformation at $T \geq T_c$ should be reflected on a symmetric optical absorbance (Mehboudi *et al.*, 2016b). In addition, and according to Shi and Kioupakis, the absorbance of $O-MX$ MLs is unusually strong in the visible range (Shi and Kioupakis, 2015).

B. Raman spectra

Raman spectroscopy is customarily employed to determine the thickness of layered materials (Castellanos-Gomez *et al.*, 2014; Li *et al.*, 2012). As indicated in Sec. II, the atomic bonds evolve with the number of layers in $O-MX$ MLs (Poudel *et al.*, 2019; Ronneberger *et al.*, 2020), which should leave signatures in the Raman spectra. Indeed, Raman modes B_{1u} , B_{2g} , A_{g^2} and B_{3g^2} are shown for monolayer and bulk SnS in Fig. 13(a), and shift as a function of the number of MLs is seen in Fig. 13(b) (Park *et al.*, 2019). Experimentally-determined Raman signatures for ultrathin SnS are displayed in Fig. 13(c) for comparison (Higashitarumizu *et al.*, 2020).

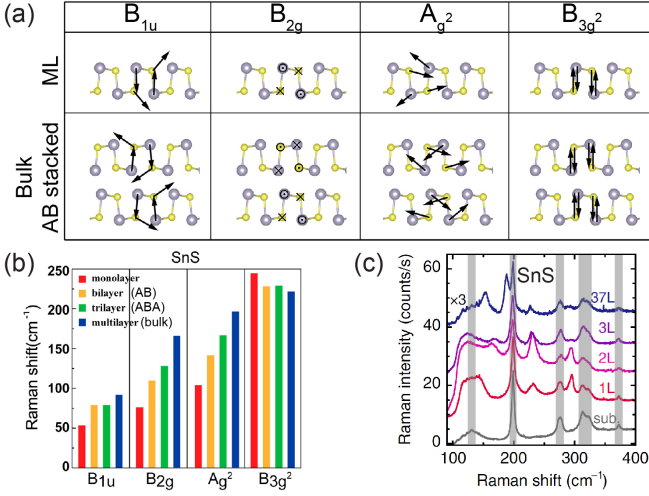


FIG. 13 (a) Relevant phonon modes for Raman spectra of ML and bulk SnS. (b) Raman shift of SnS as a function of MLs. Subplots (a) and (b) are adapted from Ref. (Park *et al.*, 2019) under the terms of the CC-BY 4.0 Attribution License. Copyright, 2020, Springer Nature. (c) Experimentally observed thickness dependence of Raman spectrum at 3 K. The peaks in the hatch are due to the substrate. From Ref. (Higashitarumizu *et al.*, 2020) under the terms of the CC-BY Attribution License. Copyright, 2020, Springer Nature.

C. Second harmonic generation

Within a semiclassical picture, the SHG originates from the non-sinusoidal motion of carriers inside crystals lacking inversion symmetry, leading to a quadratic effect in the electric field in O-MX MLs that is forbidden in the bulk. SHG is widely utilized in applications ranging from table-top frequency multipliers, surface symmetry probes, and photon entanglement in quantum computing protocols, among others (Boyd, 2020).

If the incoming electric field is homogeneous and monochromatic $E^a = E_\omega^a e^{-i\omega t} + \text{c.c.}$, the second-order polarization of the crystal oscillates at twice the driving frequency:

$$P_2^a = \sum_{bc} \chi_2^{abc}(-2\omega; \omega, \omega) E_\omega^b E_\omega^c e^{-i2\omega t} + \text{c.c.}, \quad (3)$$

where $\chi_2^{abc}(-2\omega; \omega, \omega)$ is the SHG response tensor, a is the cartesian direction of the created electric field, and b and c are the cartesian directions of the incident electric fields. Far away from the source, the irradiated field is given by $\mathbf{E} \sim \frac{d^2 \mathbf{P}_2}{dt^2}$ (Jackson, 1998).

SHG has been reported for ultrathin noncentrosymmetric samples of MoS₂ and h-BN with odd layer thicknesses (Li *et al.*, 2013). The angular dependence of SHG also reveals the rotational symmetry of the crystal lattice, and can therefore be used to determine the orientation of crystallographic axes (Attacalite *et al.*, 2015; Janisch *et al.*, 2014; Kim *et al.*, 2013; Kumar *et al.*, 2013; Li *et al.*, 2013; Malard *et al.*, 2013; Zhou *et al.*, 2015). This effect

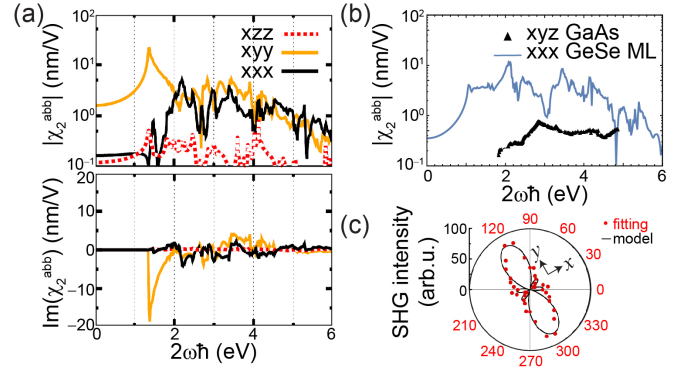


FIG. 14 (a) Absolute and imaginary SHG tensor $\chi_2^{abb}(-2\omega, \omega, \omega)$ for a SnS ML as a function of the outgoing phonon frequency 2ω . (b) Comparison between the experimental SHG tensor for GaAs(001) from (Bergfeld and Daum, 2003) and the computed one for a GeSe ML, which is an order of magnitude larger. Subplots (a) and (b) are adapted from Ref. (Panday and Fregoso, 2017) with permission. Copyright, 2017, Institute of Physics. (c) Experimental polarization dependence of SHG at 425 nm and room temperature for a SnS ML under perpendicular polarization. The inset axes show the x - and y -directions corresponding to these defined in Fig. 1(c). Reproduced from Ref. (Higashitarumizu *et al.*, 2020) under the terms of the CC-BY Attribution License. Copyright, 2020, Springer Nature.

has been theoretically (Panday and Fregoso, 2017; Wang and Qian, 2017a) and experimentally (Higashitarumizu *et al.*, 2020) studied in O-MX MLs, too.

Following the choice of axes in Fig. 1(c), the polar axis (the direction of \mathbf{P}_0) lies along the positive x -direction. Its point group only allows for non-zero xzz , xyy , xxx , yyx , zzz components of χ_2^{abc} (components obtained by exchanging the last two indices are identical, $\chi_2^{abc} = \chi_2^{acb}$). As exemplified in a SnS ML in Fig. 14(a), the SHG spectrum displays peak values within the visible spectrum that can be an order of magnitude larger than those reported for bulk GaAs (Bergfeld and Daum, 2003) [Fig. 14(b)] or for a MoS₂ ML (Malard *et al.*, 2013; Wang and Qian, 2017a). The SHG spectrum is anisotropic, and $|\chi^{xyy}| > |\chi^{xxx}| > |\chi^{zzz}|$ holds approximately true for all frequencies (Panday and Fregoso, 2017). This is a counterintuitive result, as the maximum response along the polar axis occurs for incident optical fields that are perpendicularly polarized to the polar axis.

The role of the spontaneous polarization \mathbf{P}_0 in the large SHG response tensor and in other nonlinear responses is an active area of investigation. The large magnitude of the SHG in O-MX MLs seems to be a combination of many factors, including their reduced dimensionality and in-plane polarization. Indirect evidence suggests that the in-plane \mathbf{P}_0 enhances the SHG by establishing mirror symmetries that strongly constrain contributions from certain regions within the BZ (Panday *et al.*, 2019).

O–*MX* MLs grown on insulating substrates permit performing optical experiments, and Fig. 14(c) is an experimental demonstration of the anisotropic behavior of the SHG of a SnS ML (Wang and Qian, 2017a) at room temperature, using an 850-nm laser as the excitation source (Higashitarumizu *et al.*, 2020). The largest SHG occurs along the y -axis. As discussed in Sec. IV, the sense of direction of \mathbf{P} can be set by a combination of SHG and transport measurements.

D. Bulk photovoltaic effects: injection and shift currents

The bulk photovoltaic effect (BPVE) is the generation of a dc current upon illumination in materials that lack inversion symmetry. It has been extensively studied in bulk ferroelectrics (Ivchenko and Ganichev, 2016; Sturman and Sturman, 1992), topological insulators (Hosur, 2011), 2D ferroelectrics (Kushnir *et al.*, 2019, 2017; Panday *et al.*, 2019; Rangel *et al.*, 2017), Weyl semimetals (Chan *et al.*, 2017; de Juan *et al.*, 2017; Rees *et al.*, 2019; Shvetsov *et al.*, 2019), BN nanotubes (Kral *et al.*, 2000), among other materials. Many seemingly unrelated BPVEs have been shown to have a common origin (Fregoso, 2019; Sipe and Shkrebtii, 2000). The BPVE is much larger in 2D ferroelectrics than in bulk ferroelectrics, potentially overcoming the low solar energy efficiency conversion found in the latter (Rappe *et al.*, 2017; Spanier *et al.*, 2016; Tan *et al.*, 2016).

The BPVE differs from other photovoltaic effects in three important ways: (i) it is proportional to the intensity of the optical field; (ii) it produces large open-circuit photovoltages, *i.e.*, larger than the energy band gap; and (iii) it depends on the polarization state of light. These characteristics imply, respectively, (i) that the BPVE is a second order effect in the optical field, (ii) that it is an ultrafast phenomena occurring before thermalization takes place at the CBM (VBM), and (iii) that the BPVE response tensor has a real and an imaginary component. The real component (σ_2) determines the response to linearly polarized light; the imaginary component (η_2) is the response to circularly polarized light. Denoting an homogeneous optical field by \mathbf{E} , the BPVE can then be schematically written as (Sturman and Sturman, 1992):

$$\mathbf{J}_{bpve} = \eta_2 \mathbf{E} \times \mathbf{E}^* + \sigma_2 \mathbf{E}^2. \quad (4)$$

The first term is the so-called *ballistic* current, *injection* current, or *circular photogalvanic effect*, and it vanishes for linear polarization. The injection current is created by an unequal momentum relaxation into time-reversed states (Ivchenko and Ganichev, 2016; Sturman and Sturman, 1992) or by unequal carrier pumping rates into time-reversed states $\pm \mathbf{k}$ (Fregoso, 2019; Sipe and Shkrebtii, 2000). In addition, and related to spin effects discussed in Sec. VIII.C, the chirality of circularly-polarized light couples to the spin of charge carriers to

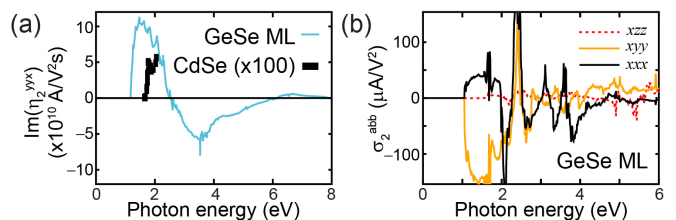


FIG. 15 (a) Injection current and (b) shift current for a GeSe ML [with axes defined as in Fig. 1(c)]. The injection current of CdSe is also plotted for comparison. Subplot (a) is adapted from Ref. (Panday *et al.*, 2019). Copyright, 2019, American Physical Society. Subplot (b) is taken from Ref. (Rangel *et al.*, 2017). Copyright, 2017, American Physical Society.

generate a spin current in spin-orbit coupled systems (Chan *et al.*, 2017; Hosur, 2011; Sturman and Sturman, 1992). Fig. 15(a) shows the spectrum of the injection current tensor for a GeSe ML. The only non-zero component is η_2^{yy} and, as a consequence, injection current can only flow perpendicularly to the polar (x) axis. The injection current tensor η_2 reaches peak values of 10^{11} A/V²s in the visible spectrum (1.5 – 3 eV) (Panday *et al.*, 2019), which is many orders of magnitude larger than its peak value in MoS₂ MLs (Arzate *et al.*, 2016).

The second term in Eqn. (4) is the *shift* current, also known as the *linear photogalvanic effect*, and its microscopic interpretation is still under debate. A popular interpretation is that the shift current arises from a shift of the electron in real-space when it absorbs a photon (von Baltz and Kraut, 1981). This is reasonable since the Wannier centers of charge are spatially separated in materials that break inversion symmetry. In a second interpretation, the quantum coherent motion of a pair of dipoles moving in k -space originates shift currents (Fregoso, 2019), which vanish for incident circularly polarized light. Fig. 15(b) shows the shift-current spectra for a GeSe ML. There is a broad maximum of the order of $150 \mu\text{A}/\text{V}^2$ (Rangel *et al.*, 2017) in the visible range (1 – 3 eV) that is larger than its magnitude in prototypical materials [*e.g.*, $\sigma_2 \sim 0.1 \mu\text{A}/\text{V}^2$ in BiFeO₃ (Young and Rappe, 2012)]. These results demonstrate the unique potential of O–*MX* MLs for optoelectronic applications.

E. Photostriction

Photostriction is the structural change induced by a screened electric polarization \mathbf{P} resulting from photoexcited electronic states: optical excitations will lead to a concurrent compression of lattice vector \mathbf{a}_1 and a comparatively smaller increase of \mathbf{a}_2 for an overall reduction in the unit cell area. The structural change documented for SnS and SnSe MLs is 10 times larger than that observed in bulk ferroelectric BiFeO₃, making O–*MX* MLs an ultimate platform for this effect (Haleoot *et al.*, 2017).

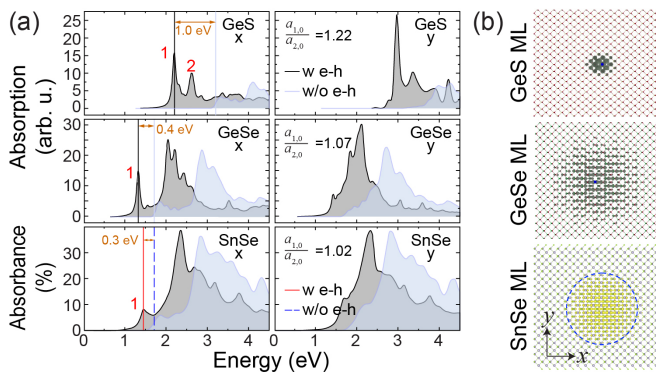


FIG. 16 (a) Absorption spectra of GeS, GeSe, and SnSe MLs with (w $e-h$) and without (w/o $e-h$) electron-hole interactions for light polarized along the x -direction (*i.e.*, parallel to \mathbf{P}_0) or along the y -direction (perpendicular to \mathbf{P}_0). Two peaks are identified for GeS MLs: peak 1 arises from a direct transition at the Γ -point, and peak 2 from a direct transition at the V_x valley (see Figure 9). For both GeSe and SnSe MLs, the only excitation within the band gap corresponds to a direct transition at the V_x valley. (b) Subplots for GeS and GeSe MLs were adapted from Ref. (Gomes *et al.*, 2016). Copyright, 2016, American Physical Society. The subplots for the SnSe ML were adapted from Ref. (Shi and Kioupakis, 2015). Copyright, 2015, American Chemical Society.

F. Excitons

An exciton is an electron-hole pair hosted within a material, whose description therefore goes beyond the single-particle picture employed thus far. Excitons display a strong dependency on dimensionality, being more strongly bound in low-dimensional systems due to a reduced Coulomb screening, and hence relevant for applications at room temperature (Gomes *et al.*, 2016). Upon laser irradiation, a MoS₂ ML displays isotropic excitons with a binding energy of 0.55 eV on a graphitic substrate (Splendiani *et al.*, 2010; Ugeda *et al.*, 2014). In turn, anisotropic excitons in BP MLs have been shown to have a larger binding energy of 0.8-0.9 eV (Rodin *et al.*, 2014a; Tran *et al.*, 2014; Wang *et al.*, 2015). Possible optoelectronic applications of O- MX MLs also call for a deep understanding of excitons (Gomes *et al.*, 2016). Given that they contribute to the dielectric environment, substrates in which 2D materials are placed may need to be accounted for when comparing experiment and theory.

The exciton binding energy has been calculated for freestanding GeS, GeSe, and SnSe MLs. It increases from less than 0.01 eV in the bulk to 1.00 eV on a GeS ML, 0.32-0.40 eV on a GeSe ML, and 0.27-0.30 eV in a SnSe ML. As seen in Fig. 16(a), the binding energy is larger in materials with small Z , for which the absorbance is more anisotropic when shining light with polarization along the x - or y - directions (Gomes *et al.*, 2016; Shi and Kioupakis, 2015). Concomitant with a stronger binding and anisotropic absorbance, lighter O- MX MLs host

more localized and anisotropic excitons [see Fig. 16(b)]. An analytical, Mott-Wannier model has been employed to account for the effect of the supporting substrate—which in general lowers the exciton binding energy—in Ref. (Gomes *et al.*, 2016).

X. SUMMARY AND OUTLOOK

Two-dimensional and ultrathin multiferroics are gaining increased attention. They complement two-dimensional semimetal graphene, insulator hexagonal boron nitride, a large number of 2D semiconductors, and two-dimensional magnets. This Colloquium describes the structural, mechanical, electronic, and optical properties of group-IV monochalcogenide MLs in a comprehensive manner, including recent developments such as the experimental realization of SnS and SnSe MLs, and novel theoretical results such as spin helix behavior, theoretical Raman spectra, and bulk photovoltaic effects, to become the most up-to-date reference on these materials. While there are a number of challenges still to be resolved concerning chemical stability, exfoliation or growth, and their stacking into functional layered materials, these ultrathin ferroelectric and ferroelastic materials have already diversified and enriched the library of layered and two-dimensional functional materials. Their prospective use in memory, valley, and optoelectronic applications can provide the motivation and justification to drive further progress in this area.

ACKNOWLEDGMENTS

We thank P. Kumar, L. Bellaiche, J. E. Moore, L. V. Titova, T. Rangel and L. Fu. S.B.-L. and J.W.V. acknowledge funding from the US Department of Energy, Office of Basic Energy Sciences (Early Career Award DE-SC0016139) and DOE-NERSC contract No. DE-AC02-05CH11231. S.S.P.P. and K.C. were supported by Deutsche Forschungsgemeinschaft (DFG, German Research Foundation), Project number PA 1812/2-1.

REFERENCES

- Absor, M. A. U., and F. Ishii (2019), *Phys. Rev. B* **100**, 115104.
- Ai, H., X. Ma, X. Shao, W. Li, and M. Zhao (2019), *Phys. Rev. Mater.* **3**, 054407.
- Almahmoud, E., I. Kornev, and L. Bellaiche (2010), *Phys. Rev. B* **81**, 064105.
- Almahmoud, E., Y. Navtsenya, I. Kornev, H. Fu, and L. Bellaiche (2004), *Phys. Rev. B* **70**, 220102.
- Amorim, B., A. Cortijo, F. de Juan, A. Grushin, F. Guinea, A. Gutierrez-Rubio, H. Ochoa, V. Parente, R. Roldn, P. San-Jose, J. Schiefele, M. Sturla, and M. Vozmediano (2016), *Phys. Rep.* **617**, 1.

- Arzate, N., B. S. Mendoza, R. A. Vázquez-Nava, Z. Ibarra-Borja, and M. I. Álvarez-Núñez (2016), *Phys. Rev. B* **93**, 115433.
- Asaba, T., Y. Wang, G. Li, Z. Xiang, C. Tinsman, L. Chen, S. Zhou, S. Zhao, D. Laleyan, Y. Li, Z. Mi, and L. Li (2018), *Sci. Rep.* **8**, 6520.
- Attaccalite, C., A. Nguer, E. Cannuccia, and M. Grüning (2015), *Phys. Chem. Chem. Phys.* **17**, 9533.
- von Baltz, R., and W. Kraut (1981), *Phys. Rev. B* **23**, 5590.
- Bao, Y., P. Song, Y. Liu, Z. Chen, M. Zhu, I. Abdelwahab, J. Su, W. Fu, X. Chi, W. Yu, W. Liu, X. Zhao, Q.-H. Xu, M. Yang, and K. P. Loh (2019), *Nano Lett.* **19**, 5109.
- Barraza-Lopez, S., T. P. Kaloni, S. P. Poudel, and P. Kumar (2018), *Phys. Rev. B* **97**, 024110.
- Bergfeld, S., and W. Daum (2003), *Phys. Rev. Lett.* **90**, 036801.
- Berland, K., V. R. Cooper, K. Lee, E. Schröder, T. Thonhauser, P. Hyldgaard, and B. I. Lundqvist (2015), *Rep. Prog. Phys.* **78**, 066501.
- Berland, K., and P. Hyldgaard (2014), *Phys. Rev. B* **89**, 035412.
- Bernevig, A. B., and T. L. Hughes (2013), *Topological Insulators and Topological Superconductors*, 1st ed. (Princeton U. Press, Princeton, N.J.).
- Bernevig, B. A., J. Orenstein, and S.-C. Zhang (2006), *Phys. Rev. Lett.* **97**, 236601.
- Black, C. T., C. Farrell, and T. J. Licata (1997), *Appl. Phys. Lett.* **71**, 2041.
- Boyd, R. W. (2020), *Nonlinear Optics*, 4th ed. (Academic Press, London, U.K.).
- Bune, A. V., V. M. Fridkin, S. Ducharme, L. M. Blinov, S. P. Palto, A. V. Sorokin, S. G. Yudin, and A. Zlatkin (1998), *Nature* **391**, 874.
- Cao, T., G. Wang, W. Han, H. Ye, C. Zhu, J. Shi, Q. Niu, P. Tan, E. Wang, B. Liu, and J. Feng (2012), *Nat. Commun.* **3**, 887.
- Castellanos-Gomez, A., L. Vicarelli, E. Prada, J. O. Island, K. L. Narasimha-Acharya, S. I. Blanter, D. J. Groenendijk, M. Buscema, G. A. Steele, J. V. Alvarez, H. W. Zandbergen, J. J. Palacios, and H. S. J. van der Zant (2014), *2D Mater.* **1**, 025001.
- Chan, C.-K., N. H. Lindner, G. Refael, and P. A. Lee (2017), *Phys. Rev. B* **95**, 041104.
- Chang, K., T. P. Kaloni, H. Lin, A. Bedoya-Pinto, A. K. Pandeya, I. Kostanovskiy, K. Zhao, Y. Zhong, X. Hu, Q.-K. Xue, X. Chen, S.-H. Ji, S. Barraza-Lopez, and S. S. P. Parkin (2019a), *Adv. Mater.* **31**, 1804428.
- Chang, K., F. Küster, B. J. Miller, J.-R. Ji, J.-L. Zhang, P. Sessi, S. Barraza-Lopez, and S. S. P. Parkin (2020), *Nano Lett.* **20**, 6590.
- Chang, K., J. Liu, H. Lin, N. Wang, K. Zhao, A. Zhang, F. Jin, Y. Zhong, X. Hu, W. Duan, Q. Zhang, L. Fu, Q.-K. Xue, X. Chen, and S.-H. Ji (2016), *Science* **353**, 274.
- Chang, K., B. J. Miller, H. Yang, H. Lin, S. S. P. Parkin, S. Barraza-Lopez, Q.-K. Xue, X. Chen, and S.-H. Ji (2019b), *Phys. Rev. Lett.* **122**, 206402.
- Chang, K., and S. S. P. Parkin (2019), *APL Mater.* **7**, 041102.
- Chang, K., and S. S. P. Parkin (2020), *J. Appl. Phys.* **127**, 220902.
- Cheiwchanchamngij, T., and W. R. L. Lambrecht (2012), *Phys. Rev. B* **85**, 205302.
- Cui, C., W.-J. Hu, X. Yan, C. Addiego, W. Gao, Y. Wang, Z. Wang, L. Li, Y. Cheng, P. Li, X. Zhang, H. N. Alshareef, T. Wu, W. Zhu, X. Pan, and L.-J. Li (2018a), *Nano Lett.* **18**, 1253.
- Cui, C., F. Xue, W.-J. Hu, and L.-J. Li (2018b), *npj 2D Mat. Appl.* **2**, 18.
- Deng, J., Y. Liu, M. Li, S. Xu, Y. Lun, P. Lv, T. Xia, P. Gao, X. Wang, and J. Hong (2019), *Small* **16**, 1904529.
- Deslippe, J., G. Samsonidze, D. A. Strubbe, M. Jain, M. L. Cohen, and S. G. Louie (2012), *Comp. Phys. Comm.* **183**, 1269.
- Dewandre, A., M. J. Verstraete, N. Grobert, and Z. Zanolli (2019), *J. Phys.: Mater.* **2**, 044005.
- Di Sante, D., P. Barone, R. Bertacco, and S. Picozzi (2013), *Adv. Mater.* **25**, 509.
- Di Sante, D., A. Stroppa, P. Barone, M.-H. Whangbo, and S. Picozzi (2015), *Phys. Rev. B* **91**, 161401.
- Dimmock, J. O., I. Melngailis, and A. J. Strauss (1966), *Phys. Rev. Lett.* **16**, 1193.
- Ding, W., J. Zhu, Z. Wang, Y. Gao, D. Xiao, Y. Gu, Z. Zhang, and W. Zhu (2017), *Nat. Commun.* **8**, 14956.
- Dresselhaus, G. (1955), *Phys. Rev.* **100**, 580.
- Du, A., Z. Pendergrast, and S. Barraza-Lopez (2020), *J. Appl. Phys.* **127**, 234103.
- Duerloo, K.-A. N., M. T. Ong, and E. J. Reed (2012), *J. Phys. Chem. Lett.* **3**, 2871.
- Evans, J. T., and R. Womack (1988), *IEEE J. Solid-State Circuits* **23**, 1171.
- Fei, R., W. Kang, and L. Yang (2016), *Phys. Rev. Lett.* **117**, 097601.
- Fei, R., W. Li, J. Li, and L. Yang (2015), *Appl. Phys. Lett.* **107**, 173104.
- Fei, Z., T. Palomaki, S. Wu, W. Zhao, X. Cai, B. Sun, P. Nguyen, J. Finney, X. Xu, and D. H. Cobden (2017), *Nat. Phys.* **13**, 677.
- Fei, Z., W. Zhao, T. A. Palomaki, B. Sun, M. K. Miller, Z. Zhao, J. Yan, X. Xu, and D. H. Cobden (2018), *Nature* **560**, 336.
- Feuersanger, A. E., A. K. Hagenlocher, and A. L. Solomon (1964), *J. Electrochem. Soc.* **111**, 1387.
- Fong, D. D., A. M. Kolpak, J. A. Eastman, S. K. Streiffer, P. H. Fuoss, G. B. Stephenson, C. Thompson, D. M. Kim, K. J. Choi, C. B. Eom, I. Grinberg, and A. M. Rappe (2006), *Phys. Rev. Lett.* **96**, 127601.
- Fong, D. D., G. B. Stephenson, S. K. Streiffer, J. A. Eastman, O. Auciello, P. H. Fuoss, and C. Thompson (2004), *Science* **304**, 1650.
- Fregoso, B. M. (2019), *Phys. Rev. B* **100**, 064301.
- Fu, Z., M. Liu, and Z. Yang (2019), *Phys. Rev. B* **99**, 205425.
- Gao, P., Z. Zhang, M. Li, R. Ishikawa, B. Feng, H.-J. Liu, Y.-L. Huang, N. Shibata, X. Ma, S. Chen, J. Zhang, K. Liu, E.-G. Wang, D. Yu, L. Liao, Y.-H. Chu, and Y. Ikuhara (2017), *Nat. Commun.* **8**, 15549.
- Gerra, G., A. K. Tagantsev, N. Setter, and K. Parlinski (2006), *Phys. Rev. Lett.* **96**, 107603.
- Gomes, L. C., and A. Carvalho (2015), *Phys. Rev. B* **92**, 085406.
- Gomes, L. C., A. Carvalho, and A. H. Castro Neto (2015), *Phys. Rev. B* **92**, 214103.
- Gomes, L. C., P. E. Trevisanutto, A. Carvalho, A. S. Rodin, and A. H. Castro Neto (2016), *Phys. Rev. B* **94**, 155428.
- Guan, Z., H. Hu, X. Shen, P. Xiang, N. Zhong, J. Chu, and C. Duan (2019), *Adv. Electron. Mater.* **6**, 1900818.
- Haleoot, R., C. Paillard, T. P. Kaloni, M. Mehboudi, B. Xu, L. Bellaiche, and S. Barraza-Lopez (2017), *Phys. Rev. Lett.* **118**, 227401.

- Hanakata, P. Z., A. Carvalho, D. K. Campbell, and H. S. Park (2016), *Phys. Rev. B* **94**, 035304.
- Heyd, J., G. E. Scuseria, and M. Ernzerhof (2003), *J. Chem. Phys.* **118**, 8207.
- Higashitarumizu, N., H. Kawamoto, C.-J. Lee, B.-H. Lin, F.-H. Chu, I. Yonemori, T. Nishimura, K. Wakabayashi, W.-H. Chang, and K. Nagashio (2020), *Nat. Commun.* **11**, 2428.
- Hosur, P. (2011), *Phys. Rev. B* **83**, 035309.
- Hu, Y., S. Zhang, S. Sun, M. Xie, B. Cai, and H. Zeng (2015), *Appl. Phys. Lett.* **107**, 122107.
- Ivchenko, E., and S. Ganichev (2016), "Spin physics in semiconductors," Chap. 9 (Springer Verlag, Berlin).
- Jackson, J. D. (1998), *Classical Electrodynamics*, 3rd ed. (Wiley, N.Y.).
- Janisch, C., Y. Wang, D. Ma, N. Mehta, A. L. Elias, N. Perea-Lopez, M. Terrones, V. Crespi, and Z. Liua (2014), *Sci. Rep.* **4**, 5530.
- Janovec, V. (1959), *Czech. J. Phys.* **9**, 468.
- Jiang, J., and H. Park (2014), *Nat. Commun.* **5**, 4727.
- de Juan, F., A. G. Grushin, T. Morimoto, and J. E. Moore (2017), *Nat. Commun.* **8**, 15995.
- Junquera, J., and P. Ghosez (2003), *Nature* **422**, 506.
- Kaloni, T. P., K. Chang, B. J. Miller, Q.-K. Xue, X. Chen, S.-H. Ji, S. S. P. Parkin, and S. Barraza-Lopez (2019), *Phys. Rev. B* **99**, 134108.
- Kamal, C., A. Chakrabarti, and M. Ezawa (2016), *Phys. Rev. B* **93**, 125428.
- Keyes, R. W. (1953), *Phys. Rev.* **92**, 580.
- Kim, C.-J., L. Brown, M. W. Graham, R. Hovden, R. W. Havener, P. L. McEuen, D. A. Muller, and J. Park (2013), *Nano Lett.* **13**, 5660.
- King-Smith, R. D., and D. Vanderbilt (1993), *Phys. Rev. B* **47**, 1651.
- Kong, X., J. Deng, L. Li, Y. Liu, X. Ding, J. Sun, and J. Z. Liu (2018), *Phys. Rev. B* **98**, 184104.
- Kooi, B. J., and M. Wuttig (2020), *Adv. Mater.* **32**, 1908302.
- Kosterlitz, J. M. (2016), *Rep. Prog. Phys.* **79**, 026001.
- Kou, L., H. Fu, Y. Ma, B. Yan, A. D. Ting Liao, and C. Chen (2018), *Phys. Rev. B* **97**, 075429.
- Král, P., E. J. Mele, and D. Tománek (2000), *Phys. Rev. Lett.* **85**, 1512.
- Kumar, N., S. Najmaei, Q. Cui, F. Ceballos, P. M. Ajayan, J. Lou, and H. Zhao (2013), *Phys. Rev. B* **87**, 161403.
- Kushnir, K., Y. Qin, Y. Shen, G. Li, B. M. Fregoso, S. Tongay, and L. V. Titova (2019), *ACS Appl. Mater. Interfaces* **11**, 5492.
- Kushnir, K., M. Wang, P. D. Fitzgerald, K. J. Koski, and L. V. Titova (2017), *ACS Energy Lett.* **2**, 1429.
- Kwon, K. C., Y. Zhang, L. Wang, W. Yu, X. Wang, I.-H. Park, H. S. Choi, T. Ma, Z. Zhu, B. Tian, C. Su, and K. P. Loh (2020), *ACS Nano* **14**, 7628.
- Lee, C., X. Wei, J. W. Kysar, and J. Hone (2008), *Science* **321**, 385.
- Lee, H., J. Im, and H. Jin (2020), *Appl. Phys. Lett.* **116**, 022411.
- Lefebvre, I., M. A. Szymanski, J. Olivier-Fourcade, and J. C. Jumas (1998), *Phys. Rev. B* **58**, 1896.
- Li, H., Q. Zhang, C. C. R. Yap, B. K. Tay, T. H. T. Edwin, A. Olivier, and D. Baillargeat (2012), *Adv. Funct. Mater.* **22**, 1385.
- Li, W., and J. Li (2015), *Nano Res.* **8**, 3796.
- Li, Y., Y. Rao, K. F. Mak, Y. You, S. Wang, C. R. Dean, and T. F. Heinz (2013), *Nano Lett.* **13**, 3329.
- Liao, W.-Q., Y. Zhang, C.-L. Hu, J.-G. Mao, H.-Y. Ye, P.-F. Li, S. D. Huang, and R.-G. Xiong (2015), *Nat. Commun.* **6**, 7338.
- Lichtensteiger, C., J.-M. Triscone, J. Junquera, and P. Ghosez (2005), *Phys. Rev. Lett.* **94**, 047603.
- Littlewood, P. B. (1980), *J. Phys. C: Solid State Phys.* **13**, 4855.
- Liu, B., M. Niu, J. Fu, Z. Xi, M. Lei, and R. Quhe (2019a), *Phys. Rev. Mater.* **3**, 054002.
- Liu, F., L. You, K. L. Seyler, X. Li, P. Yu, J. Lin, X. Wang, J. Zhou, H. Wang, H. He, S. T. Pantelides, W. Zhou, P. Sharma, X. Xu, P. M. Ajayan, J. Wang, and Z. Liu (2016), *Nat. Commun.* **7**, 12357.
- Liu, K., J. Lu, S. Picozzi, L. Bellaiche, and H. Xiang (2018), *Phys. Rev. Lett.* **121**, 027601.
- Liu, K., W. Luo, J. Ji, P. Barone, S. Picozzi, and H. Xiang (2019b), *Nat. Commun.* **10**, 5144.
- Mak, K. F., K. He, J. Shan, and T. F. Heinz (2012), *Nat. Nanotechnol.* **7**, 494.
- Mak, K. F., C. Lee, J. Hone, J. Shan, and T. F. Heinz (2010), *Phys. Rev. Lett.* **105**, 136805.
- Mak, K. F., K. L. McGill, J. Park, and P. L. McEuen (2014), *Science* **344**, 1489.
- Malard, L. M., T. V. Alencar, A. P. M. Barboza, K. F. Mak, and A. M. de Paula (2013), *Phys. Rev. B* **87**, 201401.
- Malone, B. D., and E. Kaxiras (2013), *Phys. Rev. B* **87**, 245312.
- Martin, R. M. (2004), *Electronic Structure: Basic Theory and Practical Methods*, 1st ed. (Cambridge U. Press, Cambridge, UK).
- Mehboudi, M., A. M. Dorio, W. Zhu, A. van der Zande, H. O. H. Churchill, A. A. Pacheco-Sanjuan, E. O. Harris, P. Kumar, and S. Barraza-Lopez (2016a), *Nano Lett.* **16**, 1704.
- Mehboudi, M., B. M. Fregoso, Y. Yang, W. Zhu, A. van der Zande, J. Ferrer, L. Bellaiche, P. Kumar, and S. Barraza-Lopez (2016b), *Phys. Rev. Lett.* **117**, 246802.
- Mehta, R. R., B. D. Silverman, and J. T. Jacobs (1973), *J. Appl. Phys.* **44**, 3379.
- Merz, W. J. (1956), *J. Appl. Phys.* **27**, 938.
- Meyer, B., and D. Vanderbilt (2001), *Phys. Rev. B* **63**, 205426.
- Naumis, G. G., S. Barraza-Lopez, M. Oliva-Leyva, and H. Terrones (2017), *Rep. Prog. Phys.* **80**, 096501.
- Nordlander, J., M. Campanini, M. D. Rossell, R. Erni, Q. N. Meier, A. Cano, N. A. Spaldin, M. Fiebig, and M. Trassin (2019), *Nat. Commun.* **10**, 5591.
- Panday, S. R., S. Barraza-Lopez, T. Rangel, and B. M. Fregoso (2019), *Phys. Rev. B* **100**, 195305.
- Panday, S. R., and B. M. Fregoso (2017), *J. Phys.: Condens. Matter* **29**, 43LT01.
- Parenteau, M., and C. Carlone (1990), *Phys. Rev. B* **41**, 5227.
- Park, J.-W., S. H. Eom, H. Lee, J. L. F. Da Silva, Y.-S. Kang, T.-Y. Lee, and Y. H. Khang (2009), *Phys. Rev. B* **80**, 115209.
- Park, M., J. S. Choi, and H. Lee (2019), *Sci. Rep.* **9**, 19826.
- Peelaers, H., and C. G. Van de Walle (2012), *Phys. Rev. B* **86**, 241401.
- Peng, H., Z.-H. Yang, J. P. Perdew, and J. Sun (2016), *Phys. Rev. X* **6**, 041005.
- Perdew, J. P., K. Burke, and M. Ernzerhof (1996), *Phys. Rev. Lett.* **77**, 3865.
- Perdew, J. P., and A. Zunger (1981), *Phys. Rev. B* **23**, 5048.

- Poh, S. M., S. J. R. Tan, H. Wang, P. Song, I. H. Abidi, X. Zhao, J. Dan, J. Chen, Z. Luo, S. J. Pennycook, A. H. Castro-Neto, and K. P. Loh (2018), *Nano Lett.* **10**, 6340.
- Potts, R. B. (1952), *Math. Proc. Cambridge Philos. Soc.* **48**, 106.
- Poudel, S. P., J. W. Villanova, and S. Barraza-Lopez (2019), *Phys. Rev. Mater.* **3**, 124004.
- Qian, X., J. Liu, L. Fu, and J. Li (2014), *Science* **346**, 1344.
- Rabe, K. M., C. H. Ahn, and J.-M. Triscone, Eds. (2007), *Physics of Ferroelectrics: A Modern Perspective*, 1st ed. (Springer-Verlag Berlin Heidelberg, Berlin).
- Rangel, T., B. M. Fregoso, B. S. Mendoza, T. Morimoto, J. E. Moore, and J. B. Neaton (2017), *Phys. Rev. Lett.* **119**, 067402.
- Rappe, A. M., I. Grinberg, and J. E. Spanier (2017), *Proc. Natl. Acad. Sci. (USA)* **114** (28), 7191.
- Raty, J.-Y., M. Schumacher, P. Golub, V. L. Deringer, C. Gatti, and M. Wuttig (2019), *Adv. Mater.* **31**, 1806280.
- Rees, D., K. Manna, B. Lu, T. Morimoto, H. Borrmann, C. Felser, J. Moore, D. H. Torchinsky, and J. Orenstein (2019), “Quantized photocurrents in the chiral multifold fermion system RhSi,” ArXiv:1902.03230.
- Resta, R. (1994), *Rev. Mod. Phys.* **66**, 899.
- Rodin, A. S., A. Carvalho, and A. H. Castro Neto (2014a), *Phys. Rev. B* **90**, 075429.
- Rodin, A. S., A. Carvalho, and A. H. Castro Neto (2014b), *Phys. Rev. Lett.* **112**, 176801.
- Rodin, A. S., L. C. Gomes, A. Carvalho, and A. H. Castro Neto (2016), *Phys. Rev. B* **93**, 045431.
- Ronneberger, L., Z. Zanolli, M. Wuttig, and R. Mazzarello (2020), *Adv. Mater.* **32**, 2001033.
- Rycerz, A., J. Tworzydło, and C. W. J. Beenakker (2007), *Nat. Phys.* **3**, 172.
- Sai, N., C. J. Fennie, and A. A. Demkov (2009), *Phys. Rev. Lett.* **102**, 107601.
- Sai, N., A. M. Kolpak, and A. M. Rappe (2005), *Phys. Rev. B* **72**, 020101.
- Sallen, G., L. Bouet, X. Marie, G. Wang, C. R. Zhu, W. P. Han, Y. Lu, P. H. Tan, T. Amand, B. L. Liu, and B. Urbaszek (2012), *Phys. Rev. B* **86**, 081301.
- Schäibley, J. R., H. Yu, G. Clark, P. Rivera, J. S. Ross, K. L. Seyler, W. Yao, and X. Xu (2016), *Nat. Rev. Mater.* **1**, 16055.
- Scott, J. F., and C. A. Paz de Araujo (1989), *Science* **246**, 1400.
- Shen, H., J. Liu, K. Chang, and L. Fu (2019a), *Phys. Rev. Appl.* **11**, 024048.
- Shen, X.-W., Y.-W. Fang, B.-B. Tian, and C.-G. Duan (2019b), *ACS Appl. Electron. Mater.* **1**, 1133.
- Shen, X.-W., W.-Y. Tong, S.-J. Gong, and C.-G. Duan (2017), *2D Mater.* **5**, 011001.
- Shi, G., and E. Kioupakis (2015), *Nano Lett.* **15**, 6926.
- Shi, L.-B., M.-B. Li, X.-M. Xiu, X.-Y. Liu, K.-C. Zhang, Y.-H. Liu, C.-R. Li, and H.-K. Dong (2017), *J. Appl. Phys.* **121**, 205305.
- Shimazaki, Y., M. Yamamoto, I. V. Borzenets, K. Watanabe, T. Taniguchi, and S. Tarucha (2015), *Nat. Phys.* **11**, 1032.
- Shulenburg, L., A. Baczewski, Z. Zhu, J. Guan, and D. Tomnek (2015), *Nano Lett.* **15**, 8170.
- Shvetsov, O. O., V. D. Esin, A. V. Timonina, N. N. Kolesnikov, and E. V. Deviatov (2019), *JETP Lett.* **109**, 715.
- Singh, A. K., and R. G. Hennig (2014), *Appl. Phys. Lett.* **105**, 042103.
- Sipe, J. E., and A. I. Shkrebti (2000), *Phys. Rev. B* **61**, 5337.
- Slack, J. R., and J. C. Burfoot (1971), *J. Phys. C: Solid State Phys.* **4**, 898.
- Slawińska, J., F. T. Cerasoli, H. Wang, S. Postorino, A. Supka, S. Curtarolo, M. Fornari, and M. B. Nardelli (2019), *2D Mater.* **6**, 025012.
- Slawinska, J., F. T. Cerasoli, H. Wang, S. Postorino, A. Supka, S. Curtarolo, M. Fornari, and M. B. Nardelli (2019), *2D Mater.* **6**, 025012.
- Song, Y.-H., Z.-Y. Jia, D. Zhang, X.-Y. Zhu, Z.-Q. Shi, H. Wang, L. Zhu, Q.-Q. Yuan, H. Zhang, D.-Y. Xing, and S.-C. Li (2018), *Nat. Phys.* **9**, 4071.
- Spanier, J. E., V. M. Fridkin, A. M. Rappe, A. R. Akbashev, A. Polemi, Y. Qi, Z. Gu, S. M. Young, C. J. Hawley, D. Imbrenda, G. Xiao, A. L. Bennett-Jackson, and C. L. Johnson (2016), *Nat. Photon.* **10**, 611.
- Splendiani, A., L. Sun, Y. Zhang, T. Li, J. Kim, C.-Y. Chim, G. Galli, and F. Wang (2010), *Nano Lett.* **10**, 1271.
- Sturman, B. I., and P. J. Sturman (1992), *Photovoltaic and Photo-refractive Effects in Noncentrosymmetric Materials*, 1st ed., ferroelectricity and related phenomena, Vol. 8 (Routledge).
- Sui, M., G. Chen, L. Ma, W.-Y. Shan, D. Tian, K. Watanabe, T. Taniguchi, X. Jin, W. Yao, D. Xiao, and Y. Zhang (2015), *Nat. Phys.* **11**, 1027.
- Sutter, P., S. Wimer, and E. Sutter (2019), *Nature* **570**, 354.
- Tan, L. Z., F. Zheng, S. M. Young, F. Wang, S. Liu, and A. M. Rappe (2016), *npj Comp. Mater.* **2**, 16026.
- Tang, S., C. Zhang, D. Wong, Z. Pedramrazi, H.-Z. Tsai, C. Jia, B. Moritz, M. Claassen, H. Ryu, S. Kahn, J. Jiang, H. Yan, M. Hashimoto, D. Lu, R. G. Moore, C.-C. Hwang, C. Hwang, Z. Hussain, Y. Chen, M. M. Ugeda, Z. Liu, X. Xie, T. P. Devereaux, M. F. Crommie, S.-K. Mo, and Z.-X. Shen (2017), *Nat. Phys.* **13**, 683.
- Tenne, D. A., A. Bruchhausen, N. D. Lanzillotti-Kimura, A. Fainstein, R. S. Katiyar, A. Cantarero, A. Soukiassian, V. Vaithyanathan, J. H. Haeni, W. Tian, D. G. Schlom, K. J. Choi, D. M. Kim, C. B. Eom, H. P. Sun, X. Q. Pan, Y. L. Li, L. Q. Chen, Q. X. Jia, S. M. Nakhmanson, K. M. Rabe, and X. X. Xi (2006), *Science* **313**, 1614.
- Tenne, D. A., P. Turner, J. D. Schmidt, M. Biegalski, Y. L. Li, L. Q. Chen, A. Soukiassian, S. Trolrier-McKinstry, D. G. Schlom, X. X. Xi, D. D. Fong, P. H. Fuoss, J. A. Eastman, G. B. Stephenson, C. Thompson, and S. K. Streiffer (2009), *Phys. Rev. Lett.* **103**, 177601.
- Titova, L. V., B. M. Fregoso, and R. L. Grimm (2020), in *Chalcogenide*, Woodhead Publishing Series in Electronic and Optical Materials, edited by X. Liu, S. Lee, J. K. Furdyna, T. Luo, and Y.-H. Zhang (Woodhead Publishing).
- Tomashpolski, Y. Y. (1974), *Ferroelectrics* **7**, 253.
- Tomashpolski, Y. Y., M. A. Sevostianov, M. V. Pentegova, L. A. Sorokina, and Y. N. Venevtsev (1974), *Ferroelectrics* **7**, 257.
- Tran, V., R. Soklaski, Y. Liang, and L. Yang (2014), *Phys. Rev. B* **89**, 235319.
- Triebwasser, S. (1960), *Phys. Rev.* **118**, 100.
- Tritsarlis, G., B. Malone, and E. Kaxiras (2013), *J. Appl. Phys.* **113**, 233507.
- Tsymbal, E. Y., and H. Kohlstedt (2006), *Science* **313**, 181.
- Tuttle, B. R., S. M. Alhassan, and S. T. Pantelides (2015), *Phys. Rev. B* **92**, 235405.
- Tybell, T., C. H. Ahn, and J.-M. Triscone (1999), *Appl. Phys. Lett.* **75**, 856.

- Ugeda, M. M., A. J. Bradley, S.-F. Shi, F. H. da Jornada, Y. Zhang, D. Y. Qiu, W. Ruan, S.-K. Mo, Z. Hussain, Z.-X. Shen, F. Wang, L. S. G., and M. F. Crommie (2014), *Nat. Mater.* **13**, 1091.
- Valasek, J. (1921), *Phys. Rev.* **17**, 475.
- Vanderbilt, D. (2018), *Berry Phases in Electronic Structure Theory: Electric Polarization, Orbital Magnetization and Topological Insulators* (Cambridge University Press, Cambridge, U.K.).
- Vaughn, D. D., R. J. Patel, M. A. Hickner, and R. E. Schaak (2010), *J. Am. Chem. Soc.* **132**, 15170.
- Villanova, J. W., P. Kumar, and S. Barraza-Lopez (2020), *Phys. Rev. B* **101**, 184101.
- Wan, S., Y. Li, W. Li, X. Mao, W. Zhu, and H. Zeng (2018), *Nanoscale* **10**, 14885.
- Wang, H., Z. R. Liu, H. Y. Yoong, T. R. Paudel, J. X. Xiao, R. Guo, W. N. Lin, P. Yang, J. Wang, G. M. Chow, T. Venkatesan, E. Y. Tsybal, H. Tian, and J. S. Chen (2018a), *Nat. Commun.* **9**, 3319.
- Wang, H., and X. Qian (2017a), *Nano Lett.* **17**, 5027.
- Wang, H., and X. Qian (2017b), *2D Mater.* **4**, 015042.
- Wang, X., A. M. Jones, K. L. Seyler, V. Tran, Y. Jia, H. Zhao, H. Wang, L. Yang, X. Xu, and F. Xia (2015), *Nat. Nanotechnol.* **10**, 517.
- Wang, Y., C. Xiao, M. Chen, C. Hua, J. Zou, C. Wu, J. Jiang, S. A. Yang, Y. Lu, and W. Ji (2018b), *Mater. Horiz.* **5**, 521.
- Wu, M., and P. Jena (2018), *WIREs Comput. Mol. Sci.* **8**, e1365.
- Wu, M., and X. C. Zeng (2016), *Nano Lett.* **16**, 3236.
- Wu, S., V. Fatemi, Q. D. Gibson, K. Watanabe, T. Taniguchi, R. J. Cava, and P. Jarillo-Herrero (2018), *Science* **359**, 76.
- Wu, Z., N. Huang, Z. Liu, J. Wu, W. Duan, B.-L. Gu, and X.-W. Zhang (2004), *Phys. Rev. B* **70**, 104108.
- Xiao, D., G.-B. Liu, W. Feng, X. Xu, and W. Yao (2012), *Phys. Rev. Lett.* **108**, 196802.
- Xiao, J., H. Zhu, Y. Wang, W. Feng, Y. Hu, A. Dasgupta, Y. Han, Y. Wang, D. A. Muller, L. W. Martin, P. Hu, and X. Zhang (2018), *Phys. Rev. Lett.* **120**, 227601.
- Xu, C., Y. Nahas, S. Prokhorenko, H. Xiang, and L. Bellaiche (2020), *Phys. Rev. B* **101**, 241402.
- Xu, L., M. Yang, S. J. Wang, and Y. P. Feng (2017), *Phys. Rev. B* **95**, 235434.
- Xue, F., W. Hu, K.-C. Lee, L.-S. Lu, J. Zhang, H.-L. Tang, A. Han, W.-T. Hsu, S. Tu, W.-H. Chang, C.-H. Lien, J.-H. He, Z. Zhang, L.-J. Li, and X. Zhang (2018a), *Adv. Funct. Mater.* **28**, 183738.
- Xue, F., J. Zhang, W. Hu, W.-T. Hsu, A. Han, S.-F. Leung, J.-K. Huang, Y. Wan, S. Liu, J. Zhang, J.-H. He, W.-H. Chang, Z. L. Wang, X. Zhang, and L.-J. Li (2018b), *ACS Nano* **12**, 4976.
- Yang, C., Y. Liu, G. Tang, X. Wang, and J. Hong (2018), *Appl. Phys. Lett.* **113**, 082905.
- Yang, J.-H., Y. Zhang, W.-J. Yin, X. G. Gong, B. I. Yakobson, and S.-H. Wei (2016), *Nano Lett.* **16**, 1110.
- You, L., F. Liu, H. Li, Y. Hu, S. Zhou, L. Chang, Y. Zhou, Q. Fu, G. Yuan, S. Dong, H. J. Fan, A. Gruverman, Z. Liu, and J. Wang (2018), *Adv. Mater.* **30**, 1803249.
- Young, S. M., and A. M. Rappe (2012), *Phys. Rev. Lett.* **109**, 116601.
- Yuan, S., X. Luo, H. L. Chan, C. Xiao, Y. Dai, M. Xie, and J. Hao (2019), *Nat. Commun.* **10**, 1775.
- Zemilgotov, A. G., N. A. Pertsev, H. Kohlstedt, and R. Waser (2002), *J. Appl. Phys.* **91**, 2247.
- Zeng, H., J. Dai, W. Yao, D. Xiao, and X. Cui (2012), *Nat. Nanotechnol.* **7**, 490.
- Zhang, Y., G.-P. Li, T. Shimada, J. Wang, and T. Kitamura (2014), *Phys. Rev. B* **90**, 184107.
- Zheng, C., L. Yu, L. Zhu, J. L. Collins, D. Kim, Y. Lou, C. Xu, M. Li, Z. Wei, Y. Zhang, M. T. Edmonds, S. Li, J. Seidel, Y. Zhu, J. Z. Liu, W.-X. Tang, and M. S. Fuhrer (2018), *Sci. Adv.* **4**, eaar7220.
- Zhou, X., J. Cheng, Y. Zhou, T. Cao, H. Hong, Z. Liao, S. Wu, H. Peng, K. Liu, and D. Yu (2015), *J. Am. Chem. Soc.* **137**, 7994.
- Zhou, Y., D. Wu, Y. Zhu, Y. Cho, Q. He, X. Yang, K. Herrera, Z. Chu, Y. Han, M. C. Downer, H. Peng, and K. Lai (2017), *Nano Lett.* **17**, 5508.
- Zhu, L., Y. Lu, and L. Wang (2020), *J. Appl. Phys.* **127**, 014101.
- Zhu, Z., J. Guan, D. Liu, and D. Tománek (2015), *ACS Nano* **9**, 8284.